Materials Advances

ROYAL SOCIETY OF CHEMISTRY

PAPER

View Article Online
View Journal | View Issue

Cite this: *Mater. Adv.*, 2024, 5, 8145

Surface engineering: binary Mg,Fe-LDH·xFe_3O_4 nanocomposites for improved magnetic solid-phase extraction of pharmaceuticals from aqueous solution†

Tetiana Hubetska,[ab] Victor Demchenko[a] and Natalia Kobylinska *[a]

In this work, binary Mg,Fe-LDH·xFe_3O_4 (x = 0 to 2.0) nanocomposites were prepared *via* the *in situ* growth of Mg,Fe-layered double hydroxides (LDHs) onto magnetite nanoparticles and applied for the removal of diclofenac motives. These materials were prepared by a simple prolonged sonication method and systematically characterized by several techniques (*e.g.* XRD, VRM, SEM, FTIR, TEM, *etc.*). The XRD patterns of the magnetic nanocomposites confirm the formation of both LDHs and magnetic phases. The intricate surface functional groups of the starting components played pivotal roles in the formation of magnetic composites, according to FTIR spectra. The hexagonal plate-like morphology of the Mg,Fe-LDHs and Mg,Fe-LDH·xFe_3O_4 samples is evident from TEM data. The Mg,Fe-LDH·1.0Fe_3O_4 nanocomposite exhibited high agglomeration of the magnetite nanoparticles, which broke their layered structure. Various influencing factors (*e.g.*, concentration, pH medium, and contact time) that are known to influence the adsorption properties of materials were systematically studied to clarify the mechanism of the adsorption process. To assess the safety of the adsorbents, the effect of the adsorbed DCF on the release of metal ions from the LDHs structure was also monitored. Moreover, the Mg,Fe-LDH·xFe_3O_4 (x = 0.1 to 1.0) nanocomposites can be quickly separated from the 400 mL solution by an external NdFeB magnet before and after the magnetic solid-phase extraction process. The capacity of the magnetic nanocomposites to adsorb diclofenac increased with increasing solution pH. At 25 °C and pH = 7.5, the maximum adsorption capacities for Mg,Fe-LDH·0.1Fe_3O_4 and Mg,Fe-LDH·0.3Fe_3O_4 were 153.2 mg g^{-1} (0.48 mmol g^{-1}) and 143.2 mg g^{-1} (0.45 mmol g^{-1}), respectively, which do not exceed the capacities for the starting Mg,Fe-LDHs (158.1 mg g^{-1}). Further results indicated that the adsorption isotherm for diclofenac anion retention could be fitted to the Langmuir equation. The FTIR and XRD data indicate that organic molecules are adsorbed on the obtained materials by electrostatic and complex-forming processes without significant anion-exchange reactions. Moreover, after 3 regeneration cycles, the magnetic nanocomposites still retained a highly ordered structure and morphology with a magnetic response.

Received 11th June 2024,
Accepted 10th September 2024

DOI: 10.1039/d4ma00609g

rsc.li/materials-advances

1. Introduction

Diclofenac (2-[2-(2,6-dichloroanilino) phenyl] acetic acid, DCF)[1] and its metabolites (*e.g.*, 4′-hydroxydiclofenac (4′-OH-DCF) or 5-hydroxylated DCF (5-OH-DCF)[2]) have been frequently detected in various water sources, usually as emerging compounds,[3] because of their widespread human and veterinary use since the 1970s.[4] Most of the diclofenac-containing drugs (up to 75%) enter the surface water, groundwater and soil samples.[2] Long-term exposure to these contaminants has been shown to have a negative impact on ecosystem health and sustainability.[1] It has also been proved that DCF is not readily biodegradable.[5] Several years ago, DCF (among 17 organic compounds) was included in the watch list for European Union monitoring in different aquatic compartments (namely, effluents of wastewater, surface water, and groundwater), defined in Decision 2015/495/EU.[4]

Currently, chemists and technologists are actively investigating the determination and removal of DCF from water sources.[6] So far, many methods have been widely reported to remove emerging pollutants from aqueous solutions, such as nanofiltration,[7] photocatalysis,[8,9] and adsorption[10] as a low-cost and

[a] *A.V. Dumansky Institute of Colloid and Water Chemistry, National Academy of Sciences of Ukraine, 42 Acad. Vernadskoho Blvd, Kyiv, 03142, Ukraine. E-mail: kobilinskaya@univ.kiev.ua*
[b] *Nanomaterials and Nanotechnology Research Center (CINN-CSIC), Avda. de la Vega 4-6, El Entrego, 33940, Spain*

† Electronic supplementary information (ESI) available. See DOI: https://doi.org/10.1039/d4ma00609g

feasible option in large-scale approach. However, each method has its advantages and disadvantages. For example, photo-oxidation processes have been extensively used for the water treatment of organic compounds including pharmaceuticals, but these techniques are associated with problems such as excessive time requirements with noneffective energy consumption.

To date, many adsorptive materials (*e.g.*, clay minerals, carbon-based materials, magnetic materials, *etc.*) have been reported in the literature for pharmaceuticals removal.[10–12] Compared to other reported conventional sorbents, synthetic clays (currently known as layered double hydroxides (LDHs)) have aroused increasing attention in environmental conservation because of their low-cost and simple synthesis of layered structures.[13] Furthermore, LDHs have a greater hydrophilic character and resistance to high pH solution.[14] The sorption purification process is affected by the composition of the hydrotalcite, which determines the layer charge, the nature of the anion present in the interlayer, and the amount of water molecules in the interlayer.[13] These characteristics determine the accessibility of the anionic interlayer species. Hence, they should influence the adsorption of the anionic pollutants when using these materials as sorbents.[15] The most common types of LDHs as sorbents are Mg,Al-, Mg,Fe-LDHs.[16] These two materials stand out in water treatment processes due to their high crystallinity and the simplicity of the preparation methods.[15] Many studies have shown that under the same conditions, the crystallinity of Mg,Fe-LDHs is slightly poorer than that of the Mg,Al-LDHs. However, from a safety perspective, ($K_{sp}(Al(OH)_3) = 1.3 \times 10^{-33}$) and ($K_{sp}(Fe(OH)_3) = 4.0 \times 10^{-38}$) differ by almost five orders of magnitude.[17] Nevertheless, to some extent, unmodified LDHs exhibited low removal efficiency for contaminants owing to their limited functional groups. For example, the equilibrium adsorption capacity of Zn,Fe-LDHs, Mg,Al-LDHs (or calcined at 500 °C) and Zn,Al-LDHs to diclofenac was reported to be only 74.50 mg g^{-1},[18] 123 mg g^{-1} (or 1494 mg g^{-1}),[19] and 500 mg g^{-1},[20] respectively. At the same time, the hybrid LDHs-based materials for the carbons,[21] polymers,[22,23] clays,[24] metal oxides[20,25] and industrial wastes[26] are found to be effective in the removal of DCF from aqueous solutions.

Furthermore, the LDHs used for water treatment as sorbents are usually powders. Thus, it is difficult to separate the sorbent from a suspension without a centrifugation process.[23] This disadvantage limits the applicability of LDHs when a large number of samples are considered. In such a process, automation would be desirable. Magnetic solid phase extraction (MSPE) technology (*i.e.*, applying an external magnetic field to perform the removal and preconcentration of emerging pollutants) has attracted much attention for improving the manufacturability of the sorption process.[27] Thus, an area of increased research interest is the impartion of magnetic properties to materials to enhance the purification and preconcentration process by sorbents from aqueous solution or other liquid.[14] Introducing magnetic properties to 2D-layered materials enables effective manipulation of the powders in the aqueous solution for dispersion or separation processes.

Various types of LDHs containing magnetic nanoparticles (Fe_3O_4(mainly), γ-Fe_3O_4, MFe_2O_4 (M = Co, Mg, Mn, *etc.*)), such as Mg,Al-,[28–31] Mg,Fe-,[32] CuFeNi-,[33] Zn,Cr-,[34] and Ca,Al-LDHs,[35] have been prepared by several scientific groups. The resulting magnetic composites have been typically used for controlled drug and gene delivery,[16,31] and as heterogeneous catalysts.[29,34] At present, these composites have been explored for their applications in environmental remediation[30,32,33] and photocatalysis.[34] Currently, the study of magnetic LDHs-based materials for the removal of pharmaceuticals is still in the early stage.[35] The design of a cost-effective and eco-friendly approach for the synthesis of nanocomposites for MSPE based on LDH materials remains a challenge. Thus, understanding the removal mechanisms of organic anions on the surfaces of LDHs is important for remediating many of these pollutants in water and wastewater treatments.

In this work, a MSPE procedure based on the Mg,Fe-layered double hydroxides (Mg,Fe-LDHs) decorated with magnetite nanospheres was established and applied to the removal of pharmaceutical pollutants. The main objectives were as follows: (1) to fabricate Mg,Fe-LDH·$x$$Fe_3O_4$ nanocomposites with a molar ratio (x) from 0 to 2.0; (2) to find the suitable molar ratio of Mg,Fe-LDHs to Fe_3O_4 for effective MSPE of DCF molecules; (3) to determine the influencing factors in the MSPE experiments using the feasibilities of the magnetic nanocomposites; and (4) to evaluate the potential for sustainable application of the nanocomposites in regeneration studies. The predominant factors affecting the MSPE efficiency were taken into account, and the developed procedure was successfully applied to the preconcentration and uptake of DCF from aqueous solution.

2. Experimental part

2.1. Materials

All of the chemicals used were of analytical grade, and used without further purification. The following materials were used in this study: magnesium nitrate hexahydrate ($Mg(NO_3)_2 \cdot 6H_2O$, 98.0%), iron(II) chloride tetrahydrate (99%) (Merck), iron(III) chloride anhydrous (99%), ammonium hydroxide ($NH_3 \cdot H_2O$, 25%) (Merck), ethanol (96.0%), and urea (CH_4N_2O, 96.0%) were purchased from Sigma-Aldrich. Diclofenac sodium standard was obtained from the Center of Quality Control of Drugs, Ukraine. A stock standard solution of the drug (20 μg mL^{-1}) was prepared by dissolving appropriate amounts of diclofenac sodium in deionized water. Purified water was obtained with a Milli-Q apparatus.

111355.0100 ICP multi-element standard solution IV (Certipur® Certified Reference Material, HC73962555) 23 elements (Ag, Al, B, Ba, Bi, Ca, Cd, Co, Cr, Cu, Fe, Ga, In, K, Li, Mg, Mn, Na, Ni, Pb, Sr, Tl, Zn) in diluted HNO_3 (Suprapur® 6.5%) 1000 mg L^{-1} were obtained from Merck KGaA (Darmstadt, Germany).

Stock solutions of NO_3^-, SO_4^{2-}, and PO_4^{3-} ions were prepared using $NaNO_3$, Na_2SO_4, and Na_2HPO_4 salts (Sigma-Aldrich, 99.99%) dried at 150 °C for 3 hours and double distilled water by weight (AB-204S, Mettler Toledo). Humic acid sodium salt

($C_9H_8Na_2O_4$, tech. 50–60%, 226.139 g mol^{-1}, Thermo Scientific Chemicals) was used as humic acid (HA).

A NdFeB magnet (1.0 cm × 1.5 cm × 1.5 cm) was used for the magnetic solid phase extraction procedure.

2.2. Synthesis of the samples

2.2.1. Preparation of magnetite nanoparticles. The preparation of Fe_3O_4 magnetic nanoparticles (MNPs) by the modified co-precipitation method in ammonium media was first reported by Massart.[36] In a typical synthesis, 2.83 g of $FeCl_3$ (anhydrous) was dissolved in 80 mL of deionized water in a three-necked flask. Water was previously deoxygenated with a stream of nitrogen gas for 20 min. 1.72 g $FeCl_2{\cdot}4H_2O$ was then added and thoroughly mixed at 600 rpm in a water bath at 35 °C. When the temperature became 60 °C, 10 mL of $NH_3{\cdot}H_2O$ solution (25 wt%) was added dropwise with a separating funnel into the clear yellow solution at 800 rpm. Upon addition, the solution turned black. Then, the black mixture was aged in a 60 °C water bath for 30 min under continuous stirring. N_2 gas was continuously purged throughout the above process. Finally, Fe_3O_4 nanoparticles were collected by a magnet, and washed repeatedly with ethanol (3 times) and water (3 times). One half of the obtained Fe_3O_4 was saved in an ethanol solution at room temperature for further use. The second half was washed and dried at room temperature for characterization.

2.2.2. Preparation of Mg,Fe-LDHs plates. A pristine Mg,Fe-LDHs sample with a Mg/Fe molar ratio of 3 : 1 was prepared *via* hydrothermal method. Initially, urea (0.4000 g), $Mg(NO_3)_2{\cdot}6H_2O$ (2.2312 g) and $Fe(NO_3)_3{\cdot}9H_2O$ (1.1718 g) were dissolved in 50 mL of a water mixture. The resulting mixture was sonicated for 15 min, and transferred to a 100 mL Teflon-lined autoclave that is heated at 180 °C for 12 h. The product obtained upon cooling to room temperature was transferred into a glass. One half of the resulting product was washed into a glass up to a near-neutral pH value and dried at 50 °C for further characterization. The other half was dispersed in 25 mL of deionized water to form a stable aqueous dispersion with a required concentration of brown product for further use.

2.2.3. Synthesis of Mg,Fe-LDH·$x$$Fe_3O_4$ (x = 0.1, 0.3, 0.5, 1.0 and 2.0) nanocomposites. For the preparation of Mg,Fe-LDH·$x$$Fe_3O_4$, ($x$ = 0.3), a uniform suspension of 0.2 g Fe_3O_4 in 20 mL ethanol was prepared by sonication (15 min). Then, the prepared 0.2 g of Mg,Fe-LDHs in the above solution was sonicated again for an additional 2 h. The resulting dark brown precipitate was recuperated by magnetic separation, and washed several times with distilled water to remove any ions possibly remaining in the final product. Finally, the solution was dried at 70 °C until the ethanol was completely evaporated.

Similarly, other magnetic nanocomposites (Mg,Fe-LDH·0.1Fe_3O_4, Mg,Fe-LDH·0.5Fe_3O_4, Mg,Fe-LDH·1.0Fe_3O_4 and Mg,Fe-LDH·2.0Fe_3O_4) were prepared by varying the amount of Fe_3O_4 in the reaction mixture.

2.3. Methods of samples characterization

2.3.1. Powder XRD measurements. X-ray diffraction data were obtained using a PAN Analytical X'Pert Pro high-resolution diffractometer using Cu Kα (1.5406 Å) radiation with Ni-monochromatic filter at room temperature in the 2θ range of 5° to 80°, with a scanning speed of 0.04° s^{-1} and a step time of 10 s. The crystallite sizes of the Fe_3O_4 powders were calculated by applying the Scherrer equation[37] to the full width at half maximum (FWHM) of the (311) peak. An instrumental broadening correction was applied using a LaB_6 standard.

2.3.2. N_2 adsorption–desorption analysis. N_2 adsorption/desorption isotherms were performed at 77 K with a Micromeritics ASAP 2020 adsorption analyzer. The solids (about 0.40–0.45 g) were degassed under vacuum before measurement at 110 °C for 12 hours. The specific surface area (S_{BET}) was evaluated in the relative pressure range between 0.01–0.20. The pore distribution and pore volume were calculated using the N_2 desorption isotherms based on the Barrett–Joyner–Halenda (BJH) model.

2.3.3. Fourier transform infrared (FTIR) spectroscopy. FTIR spectra were recorded using a Thermo Nicolet Nexus 470 spectrometer. Dried samples (1 mg) were mixed with KBr powder (100 mg) in an agate mortar. The mixture was pressed into a pellet under 2 tons load for 1 min, and the spectrum was immediately recorded. A total 64 scans with a resolution of 4 cm^{-1} were used for each spectrum. The signal from a pure KBr pellet was subtracted as the background.

2.3.4. Scanning electron microscopy (SEM). The morphology of solids was evaluated with a JEOL JSM-6060S microscope. The chemical composition of the initial samples and corresponding nanocomposites was analyzed by energy-dispersive X-ray spectroscopy (EDX, FEI Quanta FEG 650) operating at 20 kV.

2.3.5. Transmission electron microscopy (TEM). The average size and morphology of the samples were determined by high-resolution transmission electron microscope (HRTEM) images (JEOL 2100F, Japan) at 200 kV. The TEM samples were prepared by coating a copper grid with a thin layer of diluted nanoparticles suspension.

2.3.6. Thermogravimetric analysis (TGA). TGA was conducted to analyze the thermal decomposition path of the studied samples using a Mettler Toledo simultaneous TGA/SDTA851 thermogravimetric analyzer. The analysis was performed in a N_2 atmosphere at a gas flow rate of 100 mL min^{-1} from ambient temperature to 1000 °C at a heating rate of 5 °C min^{-1} with a sample weight of approximately 5–7 mg. The initial and highest degradation temperatures were determined from the DTG curve.

2.3.7. Magnetic measurements. Magnetic properties of samples were measured by vibrating sample magnetometer (EV9 VSM with PPMS-14T system) at room temperature using 100 Oe s^{-1} magnetic field in driving mode with a Nb_3Sn magnet between +20 to −20 kOe longitude at 300 K, a sensitivity of 10^{-5} emu, and 0.5% accuracy. Sample preparation was carried out by filling a sample-holder that consists of a quartz cylinder of diameter 3 mm × 10 mm, and closely packed vials were mounted on the brass half tube sample holder with fused quartz paddles for magnetization measurements.

2.3.8. Point of zero charge (pH_{pzc}) procedure. The "*pH drift*" method was used to calculate the pH_{pzc} value of the solids.[38]

Briefly, 0.05 g of the sample was added to 0.01 M NaCl (25 mL) with different pH_0 (3.0–11.0). Then, the solution was set for 24 h to achieve a constant pH (pH_{final} or pH_e). Finally, the pH_{final} value of the suspensions was measured. The difference between the pH_{final} and pH_0 was plotted *versus* pH_0. The pH_{pzc} value of the sample is equal to the pH_0 on the graph at which the $\Delta pH = 0$.

2.3.9. Chemical composition of adsorbents. The chemical composition of the obtained samples was determined by XRD, EDX, TGA and spectroscopic methods. To perform elemental analysis, 20 mg of solid was dissolved in 1.0 M HNO_3 (50 mL), and stirred continuously until the solid was completely dissolved. The obtained solution was filtered out with filter paper. The filtrate was analyzed by flame atomic absorption spectroscopy (AAS) to determine the concentration of the elements present in the sample.

The ratio of crystalline phases in the magnetic nanocomposites was evaluated by XRD data using the general structure analysis system (GSAS-II software package).[39]

2.4. Analytical techniques

For all of the tests, the concentrations of metal ions in the solutions were analyzed using a flame atomic absorption spectrometer (C-115M) with an air–acetylene burner.

The UV-visible spectroscopic measurements in the present work were performed on a SPECORD® 250 Plus (Analytik Jena GmbH + Co. KG) spectrophotometer operated at a resolution of 1 nm. The measurements were carried out in a quartz cell of 10 mm path length (volume 3.0 mL). Spectral recording was carried out in absorbance units at the UV wavelength range of 190–320 nm (Fig. S1, ESI†). Absorbance peaks of the DCF solution appeared at 199 nm and 276 nm. Standard diclofenac solutions in the concentration range of 0.5–40 mg L^{-1} were employed to determine the intensity of the absorbance peak at 276 nm.[18] The calibration curve of the DCF solutions was obtained through linear fitting of the absorbance peak intensity (Fig. S2, ESI†). The all-test solutions were filtered with a 0.22 μm membrane (nylon) prior to the determination of the DCF concentration.

The pH measurements were performed using an Inolab Level 2 pH/ionomer (WTW).

2.5. Adsorption experiments

2.5.1. Optimization of procedure. The influence of the initial concentrations of DCF from 1 to 500 mg L^{-1} was examined. The adsorption experiments were performed at ambient temperature using batch method. An internal temperature control system was deemed unnecessary because the room temperature (and consequently, the temperature of the test solution) exhibited negligible change from approximately 25 ± 2 °C. The experiments were provided by adding 10–100 mg of obtained solids into 20–300 mL of diclofenac solution. After shaking at 150–180 rpm for a duration of 300 min, the mixture of solid and liquid was separated *via* NdFeB magnet (or filtration) and measured by spectrophotometry and AAS methods.

The pH of the solution was controlled from 5.0 to 11.0 *via* 0.1 M HCl and 0.1 M NaOH. Additionally, the solution pH was periodically evaluated utilizing a pH meter, and kept constant by adding drops of 0.1, 0.05 or 0.01 M HCl or NaOH solutions, as needed.

2.5.2. Adsorption kinetics. The kinetic adsorption experiments of DCF onto the obtained solids were checked at one initial concentration (300 mg L^{-1}) at room temperature. Briefly, 50 mg of adsorbent was added to 50 mL of DCF solution at pH 7.5 ± 0.1, and the mixtures were agitated on an orbital shaker at 180 rpm for various time intervals. The kinetic data were evaluated with the adsorption time from 0 to 300 min. At the predetermined time, the DCF concentrations in the solutions were assessed using spectrophotometry at 276 nm. Also, the adsorbed amount at time t (q_t) was calculated in accordance with the following equation:

$$q_t \text{ (mmol g}^{-1}) = (C_0 - C_t)\cdot V/m$$

where C_0 and C_t are the DCF concentrations in solution at the initial and each time t (min), respectively, with units of mol L^{-1}; m is the weight of adsorbent with unit g; and V is the volume of adsorbate solution with unit L.

2.5.3. Adsorption equilibrium studies. For adsorption isotherms, the procedure was performed with various initial concentrations from 10 to 500 mg L^{-1}, and the pH was adjusted to about 7.5 under batch condition. The experiment was carried out as follows: suspensions of 50 mg of Mg,Fe-LDHs (or magnetic nanocomposites) and a 50 mL solution were placed under constant stirring overnight at room temperature. When the adsorption equilibrium was reached, the adsorbents were conveniently separated *via* external magnetic field (using NdFeB magnet) and the supernatant was analyzed to allow DCF concentration measurements.

The DCF removal efficiency (R, %) and adsorption capacity (q_e, mmol g^{-1}) were calculated according to the following formula:

$$R\ (\%) = (C_0 - C_e)/C_0$$

$$q_e \text{ (mmol g}^{-1}) = (C_0 - C_e)\cdot V/m$$

where C_0 and C_e are the DCF initial and equilibrium concentrations, respectively, with units of mol L^{-1}; m is the weight of adsorbent, g; and V is the volume of the adsorbate solution, L.

2.6. Desorption (regeneration) experiments

To check the reusability of the adsorption process, the DCF-loaded adsorbents were first stirred overnight with 100 mL $NaNO_3$ (or Na_2CO_3) solution (100 mg L^{-1}). Then, the absorbance of the solution was measured to determine the concentration of released DCF. The effect of DCF release was controlled by spectrophotometry and TGA analysis. After thorough and repeated washing steps with distilled water until neutral pH, the adsorbent was magnetically separated and dried at 50 °C for the next experiments.

2.7. Release of metal ions and effect of co-existing ions

The effect of adsorbed DCF on the release of metal ions from the starting Mg,Fe-LDHs matrix was controlled using the AAS

method. The release of Mg(II) and Fe(III) ions into solution from Mg,Fe-LDH·xFe$_3$O$_4$ nanocomposites and different interferent ions was also studied.

The release of metal ions was monitored in 50-mL centrifuge tubes consisting of magnetic solids, oxygen-free double-distilled water, 100 mg L^{-1} ICP multi-element standard solution IV and a pre-determined concentration of DCF. Simultaneously, the influence of inorganic anions and humic acids (0.1 mg mL^{-1}) were also investigated under the same conditions.

2.8. Sample preparation of environmental water samples

The environmental samples (artesian, urban river and lake waters) were collected from 28 June to 05 August 2024 in Kyiv (Ukraine), from an artesian well (20 meters deep) in the city district area, Dnipro River (near the center of Kyiv), and Vira Lake (near a pharmaceutical plant). A 1-mL volume of 65% nitric acid per 1 L of the water samples was added for stabilization. The stabilized water samples were refrigerated in glass bottles at 4 °C.

Subsequently, 50 mg of magnetic adsorbent was added to 250 mL of each water sample with spiked amounts of target analyte; the pH of the suspensions was adjusted to 7.2–7.8, and it was stirred for 5 hours at room temperature. The solid phase was isolated from the suspension with the NdFeB magnet, and the target analyte and metal contents were determined in the supernatant solution by spectrophotometry and AAS methods. The water samples were filtered with a 0.45 μm membrane prior to the determination of DCF and metal ions.

3. Results and discussion

3.1. Synthesis and characterization of materials

The Mg,Fe-LDH·xFe$_3$O$_4$ (x = 0.1, 0.3, 0.5 and 1.0) nanocomposites were synthesized using a multi-step method. The illustration of the formation of the Mg,Fe-LDH·xFe$_3$O$_4$ nanocomposites is shown in Scheme 1.

In the first stage, Mg,Fe-LDHs nanoplates grew directly by hydrothermal method. Then, magnetite nanoparticles were prepared through an easy *in situ* coprecipitation approach, and used as the new nano-supports. In the second stage, Fe$_3$O$_4$ was dispersed in the Mg,Fe-LDHs suspension *via* ultrasonic agitation to obtain a uniform material. The electrostatic attraction between Fe$_3$O$_4$ and Mg,Fe-LDHs combined with ultrasonic treatment provided a strong driving force for the effective assembly of Fe$_3$O$_4$ nanoparticles on Mg,Fe-LDHs nanoplates (Scheme 1). The step-by-step reaction procedures to synthesize the magnetic nanocomposites were controlled by various instrumental methods.

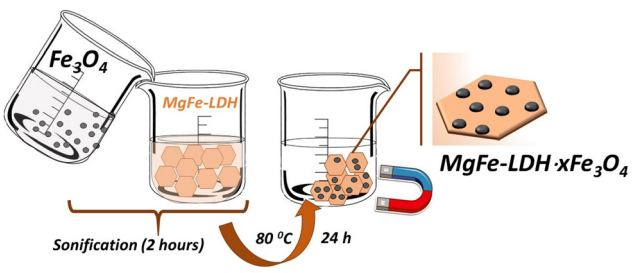

Scheme 1 Schematic presentation of the synthesis route of the Mg,Fe-LDH·xFe$_3$O$_4$ nanocomposites.

The SEM images indicated that the as-synthesized material was composed of bulk-like aggregated structures after drying (Fig. S3, ESI†). These data also reveal that the starting Mg,Fe-LDHs material and most of the nanocomposites have a classical layered structure.[19] SEM images of the magnetic nanocomposites revealed that the solid surface was also rough, and the particles agglomerated to varying extents. This might be due to the magnetic dipole moment interaction between the magnetite cores. Furthermore, TEM images were recorded to observe the morphology of all materials to be prepared, and to confirm the combination of Mg,Fe-LDHs with the Fe$_3$O$_4$ cores (Fig. 1). Mg,Fe-LDHs consist of well-dispersed plates with hexagonal morphology and sizes in a range of *ca.* 80–105 nm (Fig. 1a). The electron micrograph of the Mg,Fe-LDH·xFe$_3$O$_4$ nanocomposites shows the Mg,Fe-LDHs maintaining the external shape. However, a noticeable network of black points appears in the plate surfaces, which can be ascribed to the Fe$_3$O$_4$ nanoparticles. The average size of the Fe$_3$O$_4$ nanoparticles was *ca.* 20–25 nm. This is higher than the average diameter (10 nm) of bare Fe$_3$O$_4$ (Fig. 1b) because there was a small amount of agglomeration in several magnetic nanoparticles. It is also noteworthy that the plate morphology of the Mg,Fe-LDHs sample was found to be stable when subjected to stirring or ultrasound treatment during the preparation of the magnetic nanocomposites (Fig. 1c–e). The TEM images of the Mg,Fe-LDH·2.0Fe$_3$O$_4$ sample exhibited formed particles with irregularly shaped sheets and conglomerates of Fe$_3$O$_4$ nanoparticles on the surface of the sheets (Fig. 1f).

XRD analysis was used to determine the crystalline phase structure and purity of the prepared magnetic nanocomposites and corresponding homophases (Fig. 2). The XRD pattern of the starting Mg,Fe-LDHs exhibits a typical two-dimensional lamellar structure with rhombohedral symmetry (3R-polytype) and major diffraction peaks consistent with the (003), (006), (012) and (110) lattice planes, demonstrating the successful synthesis of crystalline hydrotalcite-like materials with the general formula $[Mg_6Fe_2(CO_3)(OH)_{16}]\cdot 4H_2O$ according to JCPDS: 38-0486. This effect indicated that the interlayer anion of the obtained Mg,Fe-LDHs was carbonate because most LDHs containing CO_3^{2-} ions had this symmetry. The diffraction pattern of the Fe$_3$O$_4$ sample matches perfectly with the spinel type phase (250540-ICSD), with the main diffraction peaks consistent with the (220), (311), (222), (400), (422), (511), (440) and (533) lattice planes. Crystalline phases of impurities were not observed. All diffraction peaks of Mg,Fe-LDHs and Fe$_3$O$_4$ nanoparticles can be observed in the Mg,Fe-LDH·0.3Fe$_3$O$_4$ samples. This confirms the formation of the magnetic nanocomposites. The (003) peak intensity of Mg,Fe-LDHs coincides with the highly intense peak of Fe$_3$O$_4$. It should be noted here that the main (003) peak of the harmonica-like 2D-structure of Mg,Fe-LDHs phase is higher in intensity compared to the (311) peak of magnetite. Therefore, it is understood that the fraction

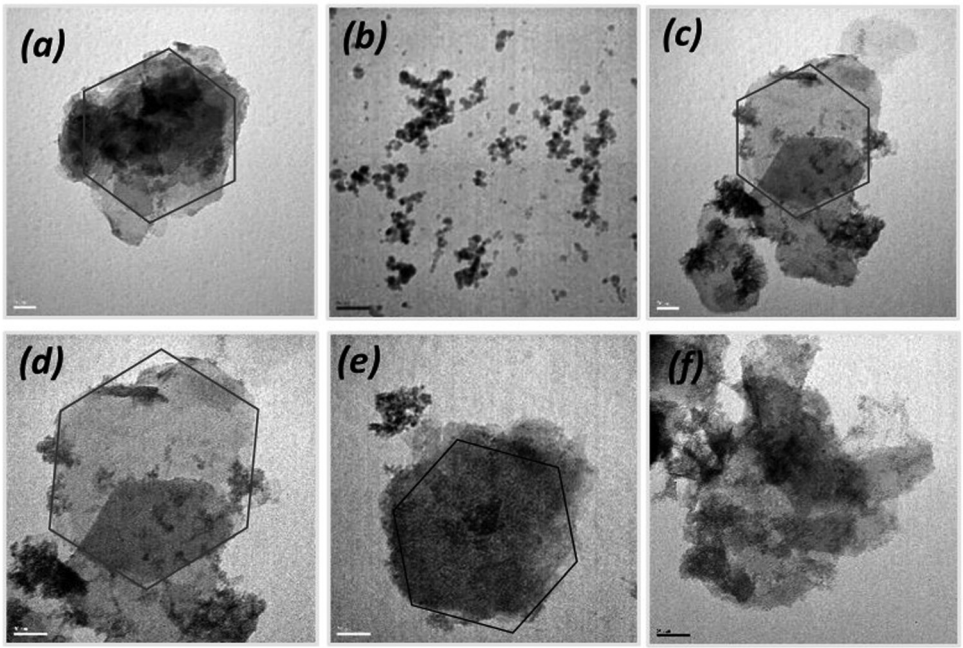

Fig. 1 TEM images of Mg,Fe-LDHs (a), Fe_3O_4 (b), Mg,Fe-LDH·0.1Fe_3O_4 (c), Mg,Fe-LDH·0.3Fe_3O_4 (d), Mg,Fe-LDH·0.5Fe_3O_4 (e), and Mg,Fe-LDH·2.0Fe_3O_4 (f) samples.

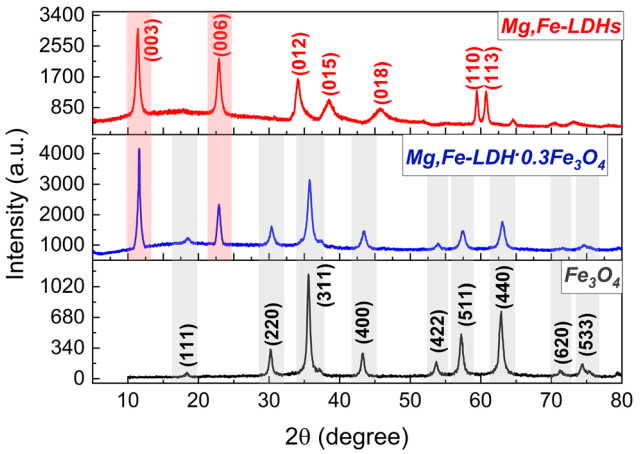

Fig. 2 Powder XRD patterns of the initial components (Fe_3O_4 and Mg,Fe-LDHs) and the resulting magnetic nanocomposite (Mg,Fe-LDH·0.3Fe_3O_4).

Table 1 Crystal lattice parameters of the synthesized samples according to XRD analysis

	Magnetite	Hydrotalcite			
Sample	$D_{(311)}$, Å	$d_{(003)}$, Å	$a = b$, Å	c, Å	$D_{(003)}$, Å
Mg,Fe-LDHs	—	7.7761	3.1095	23.3284	33.5
Mg,Fe-LDH·0.1Fe_3O_4	*14.2*	7.7763	3.1098	23.3296	20.2
Mg,Fe-LDH·0.3Fe_3O_4	*13.3*	7.7769	3.1101	23.3298	32.2
Mg,Fe-LDH·0.5Fe_3O_4	*12.5*	7.7773	3.1107	23.3310	21.2
Mg,Fe-LDH·1.0Fe_3O_4	*14.0*	7.7784	3.1121	23.3423	36.7
Mg,Fe-LDH·2.0Fe_3O_4	*14.2*	7.7923	3.1045	23.3331	25.5
Fe_3O_4	12.2	—	—	—	—

Notes. $a = 2d_{(110)}$ and represents the average distance between cations; $c = 3d_{(003)}$ and is related to the thickness of the interlayer distance.

of Fe_3O_4 is lower than Mg,Fe-LDHs. The increase in the formation of the magnetic phase is due to the addition of a higher concentration of magnetite, leading to the formation of aggregates, which broke the layered structure of the magnetic nanocomposite (Mg,Fe-LDH·2.0Fe_3O_4 sample). However, by increasing the stoichiometry of Fe_3O_4 in the magnetic nanocomposites, the relative intensities of the diffraction peaks corresponding to Fe_3O_4 start to uncontrollably increase. It has been also confirmed that no changes occur when varying the amount of magnetite phase in the crystalline layered structure before $x = 1.0$ (Fig. S4, ESI†).

The crystal lattice parameters of the obtained materials were calculated from the XRD data (Table 1). Parameter a represents the average intermetallic distance calculated from the position of the (110) reflection, and parameter c corresponds to $3d_{(003)}$. The basal spacing of the starting Mg,Fe-LDHs equals 7.7761 Å based on the (003) plane. The $d_{(003)}$ values of the obtained magnetic nanocomposites were found to range from 7.7763 Å to 7.7923 Å. The crystallite sizes (D, Å) for the Fe_3O_4 and Mg,Fe-LDH·$x$$Fe_3O_4$ samples were determined by Scherrer equation[37] from the characteristic peaks (311) and (003) of the crystal plane Fe_3O_4 and Mg,Fe-LDHs phases, respectively. These XRD results are consistent with those reported in the literature for these compounds prepared by other routes.[15]

Fig. 3a shows the magnetic hysteresis loops of the Fe_3O_4 nanoparticles and the corresponding magnetic nanocomposites. All of the obtained samples present superparamagnetic properties. The synthesized magnetic nanocomposites have almost zero coercivity and remanence, thus proving their superparamagnetic properties.[40] These properties of the

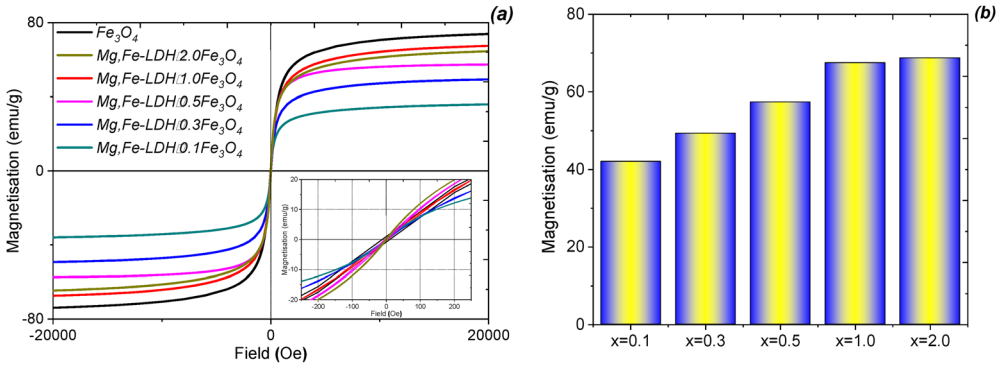

Fig. 3 Magnetic hysteresis loops (a) and variation of the magnetizations (b) for the Fe_3O_4 and Mg,Fe-LDH·xFe_3O_4 (x = 0 to 2) samples.

nanocomposites can be explained in that the Fe_3O_4 nanoparticles consist of small crystallite aggregates, which have LDHs shells around each other. The saturation magnetization of pristine Fe_3O_4 is 75.87 emu g^{-1}, which is lower than that of the bulk magnetite (92 emu g^{-1}).[41] Upon increasing the stoichiometric ratio of Fe_3O_4, the specific saturation magnetizations of the magnetic nanocomposites initially linearly increases and then levels off (Fig. 3b). This might be due to the bonding of the diamagnetic materials (inorganic layered materials) to the nanoparticles surface, hence quenching their magnetic moment. In addition, the disordered surface region of the prepared magnetic nanoparticles increases the surface spin disorientation. This might lead to the reduction of the effective magnetic moment. Conversely, the saturation magnetization of the highest Fe_3O_4-loading nanocomposite (Mg,Fe-LDH·2.0Fe_3O_4) is 67.49 emu g^{-1}, which is below the value obtained for pristine Fe_3O_4. The magnetic nanocomposite with x = 0.1 has the lowest magnetization (38.03 emu g^{-1}), which is ~2 times less compared to the pristine magnetite; it still can be used even under a relatively low external magnetic field.

The pristine Fe_3O_4 can be separated quickly and efficiently under a magnetic field in just 10 s, and re-dispersed immediately once the external magnetic field is off. Although the magnetization of Mg,Fe-LDH·xFe_3O_4 decreases as a result of functionalization, the magnetic responses of Mg,Fe-LDH·0.3Fe_3O_4 and Mg,Fe-LDH·0.5Fe_3O_4 are sufficiently high for practical applications. This confirmed that Fe_3O_4 and Mg,Fe-LDHs were assembled into the nanocomposites, rather than just mechanically mixed.

The textural parameters of the materials are a very important characteristic in the adsorption process. In this way, the specific surface area (S_{BET}), the total pore volume (V_{tot}), and pore size distribution (D) of the obtained solids are measured using N_2 adsorption/desorption at 77 K (Fig. 4).

As presented in Fig. 4a, the adsorption/desorption isotherms of the Mg,Fe-LDHs and corresponding magnetic nanocomposites are of type II, according to the IUPAC classification.[42] The isotherms exhibit a low closed H3-type hysteresis loop above the relative pressure of 0.6 due to the mesopores structure and capillary condensation process, accompanied by multilayers when starting the adsorptive cycle.

The N_2 adsorption/desorption data show that the S_{BET} of the bare Mg,Fe-LDHs is 120.0 m^2 g^{-1} (Table 2), which is greater than that reported by Silva *et al.* (84.0 m^2 g^{-1}).[15] Quite differently, the specific surface area of bare Fe_3O_4 is less than 50 m^2 g^{-1} and there is a very narrow distribution of the pore size (4.0 nm), as shown in Fig. 4b. At the same time, all magnetic layer-structured nanoadsorbents show a lower S_{BET} than bare Mg,Fe-LDHs. The Mg,Fe-LDH·0.1Fe_3O_4 nanocomposite has a specific surface area of 108.4 m^2 g^{-1} and a broad pore

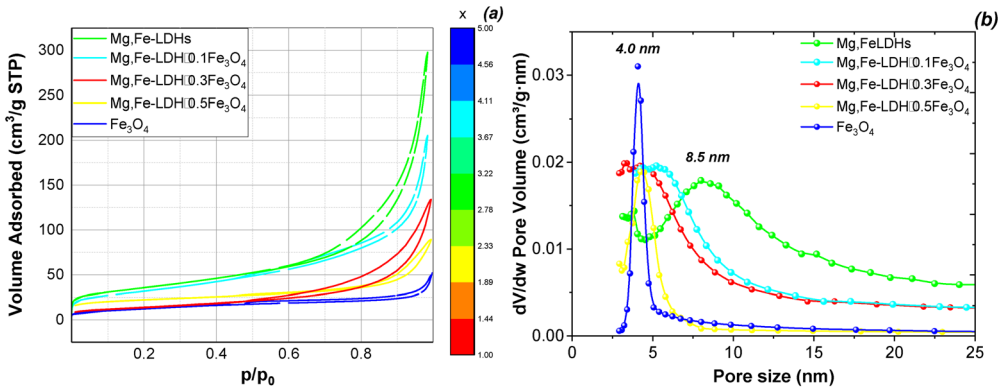

Fig. 4 N_2 adsorption/desorption isotherms (a) and pore size distribution (b) of the initial components and corresponding magnetic nanocomposites.

Table 2 The textural properties of Mg,Fe-LDHs and other magnetic materials

Samples	S_{BET} (m^2 g^{-1})	V_{tot} (cm^3 g^{-1})	D (nm)
Mg,Fe-LDHs	120.0	0.21	8.54
Mg,Fe-LDH·0.1Fe_3O_4	108.4	0.20	6.23
Mg,Fe-LDH·0.3Fe_3O_4	70.3	0.19	5.72
Mg,Fe-LDH·0.5Fe_3O_4	65.0	0.18	4.97
Mg,Fe-LDH·1.0Fe_3O_4	45.0	0.18	4.07
Fe_3O_4	42.0	0.17	4.05

size distribution of 6.0–6.3 nm, while the Mg,Fe-LDH·0.5Fe_3O_4 sample has a S_{BET} of 45.0 m^2 g^{-1} and a narrow pore size distribution close to 4.07 nm. These results are in agreement with the different morphologies of the nanocomposites, *i.e.*, Mg,Fe-LDH·0.5Fe_3O_4 with the compact parallel stacking Mg,Fe-LDHs shell plates may possess a small S_{BET} compared to Mg,Fe-LDH·0.1Fe_3O_4 with relatively loose vertically oriented Mg,Fe-LDHs shell plates.

The FTIR spectra of the starting components (Mg,Fe-LDHs and Fe_3O_4) and corresponding magnetic nanocomposites (Mg,Fe-LDH·0.3Fe_3O_4 as example) are illustrated in Fig. 5. The strong and broad absorption peak in all FTIR spectra between 3600 and 3300 cm^{-1} is due to the hydrogen-bonded ν(OH) vibrations, both from the brucite-like layers and from the interlayer water molecules. The interlayer water molecules also give rise to the broad absorption vibration ($\delta(H_2O)$) with medium intensity that is close to 1630 cm^{-1}. Moreover, the hydrogen bonding of the water with interlayer CO_3^{2-} ions also gives rise to a shoulder at 1354 cm^{-1} in the spectrum of the Mg,Fe-LDHs sample. The very intense absorption band at 1361 cm^{-1} in the Mg,Fe-LDH·0.3Fe_3O_4 spectrum corresponds to the ν_3 mode of the interlayer CO_3^{2-} species. Thus, this band was shifted to higher wavenumbers after contact with magnetite nanoparticles. Furthermore, when compared to ν(OH) of H_2O molecules, the strong and narrow band of $\nu_3(CO_3^{2-})$ for Mg,Fe-LDHs compared to Mg,Fe-LDH·0.3Fe_3O_4 indicates a higher symmetry of the arrangement of interlayer CO_3^{2-} ions between the layers of Mg,Fe-LDHs, and thus higher crystallinity of that sample.

For all samples, the stretching modes at shorter frequency (below 800 cm^{-1}) are due to lattice vibrations, involving metal–oxygen stretching bonds (Fig. 5). The peaks located at 739 cm^{-1} and 584 cm^{-1} shown in the spectrum of Mg,Fe-LDHs are the stretching vibration of the Mg(II)–O and Fe(III)–O bonds of brucite-like layers, respectively. Furthermore, the FTIR spectrum of the Fe_3O_4 nanoparticles shows two typical bands of Fe–O bonds: one at about 428 cm^{-1} that is attributed to the stretching modes of the octahedral sites of the Fe(II)–O bonds, and the other at about 578 cm^{-1} that is attributed to the stretching vibrations of the octahedral and tetrahedral sites (Fe(III)–O). These vibrations were shifted to higher wavenumbers to 445 cm^{-1} and 584 cm^{-1}, respectively, after the Fe_3O_4 was loaded onto the Mg,Fe-LDHs. Furthermore, there was a new band observed at 570 cm^{-1}, which was assigned to the Fe(III)–O stretching vibration of Fe_3O_4. The M–O vibrational modes of the magnetic nanocomposites that lie below 1000 cm^{-1} are shifted in position in association with the different atomic weights of the Mg(II), Fe(II) and Fe(III) ions and their bond strengths with oxygen. The 1380 cm^{-1} band shifted to a higher wavenumber (1438 cm^{-1}), which is attributed to the interaction between Fe_3O_4 and the interlayer anions of Mg,Fe-LDHs. Thus, the FTIR spectrum of the Mg,Fe-LDH·0.3Fe_3O_4 sample indicates a mixture of MgFe-LDHs and Fe_3O_4 phases.

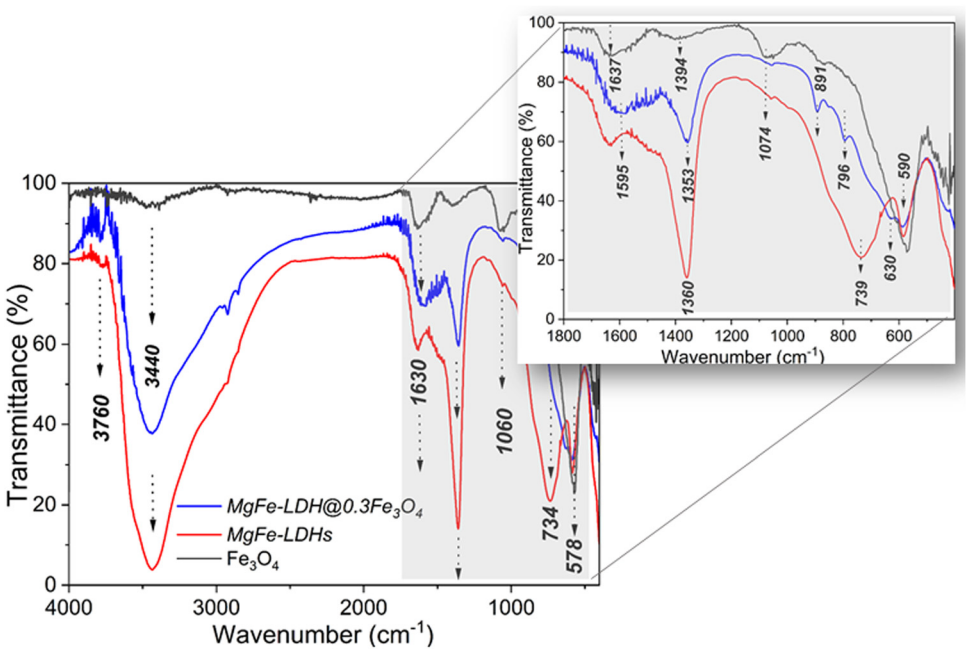

Fig. 5 FTIR spectra of the initial components and corresponding magnetic nanocomposite.

Table 3 The chemical compositions of the prepared materials based on EDX and AAS analyses

	EDX analysis				AAS analysis			
	Composition (%)							
Sample	Mg(II)	Fe(III)	Cl(I)	Mg(II)/Fe(III)	Mg(II)	Fe(III)	Na(I)	Mg(II)/Fe(III)
Mg,Fe-LDHs	55.2	—	15.2	—	51.4	17.7	12.1	2.9
Mg,Fe-LDH·0.1Fe_3O_4	41.3	34.3	13.2	0.95	32.15	14.06	10.6	1.24
Mg,Fe-LDH·0.3Fe_3O_4	21.1	22.9	3.11	1.12	21.13	24.11	8.51	1.12
Mg,Fe-LDH·0.5Fe_3O_4	31.1	26.1	14.3	1.19	33,4	43.8	5.26	0.76
Mg,Fe-LDH·1.0Fe_3O_4	22.1	21.4	9.3	1.05	21,3	39.5	1.29	0.85

EDX, AAS and TGA analyses were combined to obtain the chemical composition of the prepared solids. The EDX spectra in Fig. S4 (ESI†) demonstrated the presence of O, Mg, Fe, Na and Cl elements in Mg,Fe-LDHs. Of these, Na and Cl are attributed to several impurities, and Mg, Fe, and O are derived from the target Mg,Fe-LDHs sample. It can be seen from Table 3 that the Mg(II)/Fe(III) molar ratios of the Mg,Fe-LDHs was about 2.9, which was equal to those of the starting reaction mixture (3.0), suggesting complete coprecipitation of the metal cations on the brucite layers during hydrothermal treatment. However, the molar ratios of the samples by both methods are quite different. The Mg(II)/Fe(III) ratios by EDX analysis are obviously lower than the AAS one, indicating the possible Fe_3O_4-rich surface of the sorbents. Meanwhile, the Mg(II)/Fe(III) molar ratios of Mg,Fe-LDH·0.1Fe_3O_4 and Mg,Fe-LDH·0.5Fe_3O_4 are much larger than the corresponding AAS ones (0.76 and 0.15). For Mg,Fe-LDHs, the Mg(II) species is even undetected on the surface owing to its much thicker Fe_3O_4 layer, as mainly illustrated by the TEM data (Fig. 1c–f). These observations clearly demonstrate the clear structure of these magnetic nanoadsorbents involving the Mg,Fe-LDHs plate-like particles with different amounts of variously oriented growth of the magnetic nanoparticles on their surface.

The TGA analysis of the as-synthesized materials was performed under an inert atmosphere (Fig. 6). The total weight loss of the bare Fe_3O_4 is 4.4% (Fig. 6a) for the whole temperature range because of the slow removal of all kinds of adsorbed water. Accordingly, the TG curves of the Mg,Fe-LDHs and Mg,Fe-LDH·0.3Fe_3O_4 samples exhibit four degradation steps. The first step corresponds to the removal of physically bonded water from the interlayer space (25–170 °C), and a weight loss of 8.8% is observed on both TG curves for this stage. The second one (in the temperature interval of 170–340 °C) is related to the dehydration of the brucite-like layers, where the TG curve shows a major weight loss of 8.7%. The next weigh loss of 13.8% also occurred at the temperature range of 340–530 °C, which is due to the decomposition of the interlayer carbonate ions. The last weight loss of 8.9% occurred at high temperature (≥530 °C), and can be ascribed to the dehydroxylation (or the collapse) of the hydroxide layers. The total weight losses of the prepared Mg,Fe-LDHs and Mg,Fe-LDH·0.3Fe_3O_4 samples were measured to be 40.2% and 34.7%, respectively.

As in Fig. 6b, the DTA profile of the samples shows three main peaks at 120 °C, 270 °C and 395 °C (and an edge at 550 °C). The peaks at 165 °C and the edge of 270 °C originated from the interlayer water loss and dehydration, respectively. The peak at 395 °C can be ascribed to the dehydroxylation and decomposition of anionic carbonates. Generally, the mass loss processes were endothermic, thus supporting a water vaporization mechanism. The DTA results for the initial Mg,Fe-LDHs were similar to those of the magnetic nanocomposite.

To complete the characterization study, the stoichiometric coefficients of the materials were derived using the Mg/Fe ratio determined by AAS (Table 3), the amount of CO_2 and H_2O lost between 250 °C and 800 °C determined by TGA (Fig. 6a), and considering the electroneutrality of the solids. The uncertainties are based on the assumption that the analytical accuracy of the used AAS technique is ±5% for Mg and Fe, and that the

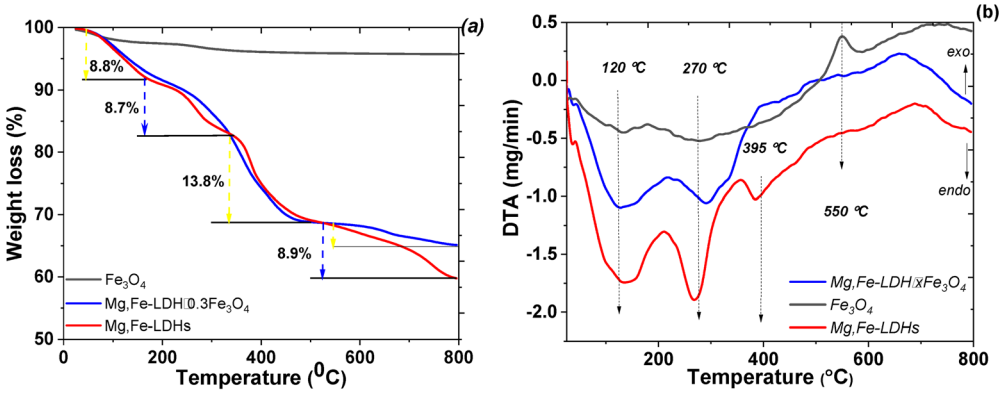

Fig. 6 TG (a) and DTA (b) curves of the Fe_3O_4, Mg,Fe-LDHs and Mg,Fe-LDH·0.3Fe_3O_4 samples.

trueness of the TGA analysis is well below 5%. In this case, for sample Mg,Fe-LDH·0.3Fe_3O_4 containing carbonate ions, the following formula $Mg_{0.74}Fe_{0.26}(OH)_2[(CO_3^{2-})_{0.2}{\cdot}2H_2O]{\cdot}0.3(Fe_3O_4)$ is calculated.

To identify the chemical composition and phases formed from the solids, the solids obtained upon TGA of Mg,Fe-LDH·0.3Fe_3O_4 at temperatures ranging from 100 to 800 °C were also analyzed by XRD analysis (Fig. S5, ESI†). The products can be indexed to $MgFe_2O_4$ (spinel phase), MgO, and FeO, and the removal of interlayer water, hydroxyl and carbonate groups can be described as follows:

1st stage:

$$Mg_{0.74}Fe_{0.26}(OH)_2[(CO_3^{2-})_{0.2}{\cdot}2H_2O]{\cdot}0.3(Fe_3O_4) \rightarrow Mg_{0.74}Fe_{0.26}(OH)_2[(CO_3^{2-})_{0.2}]{\cdot}0.3(Fe_3O_4) + 2H_2O$$

2nd stage:

$$Mg_{0.74}Fe_{0.26}(OH)_2[(CO_3^{2-})_{0.2}]{\cdot}0.3(Fe_3O_4) \rightarrow Mg_{0.74}Fe_{0.26}O[(CO_3^{2-})_{0.2}]{\cdot}0.3(Fe_3O_4) + H_2O$$

3rd stage:

$$Mg_{0.74}Fe_{0.26}O[(CO_3^{2-})_{0.2}]{\cdot}0.3(Fe_3O_4) \rightarrow Mg_{0.72}Fe_{0.28}O(Fe_3O_4)_{0.3} (or(MgO)_{0.37}(FeO)_{0.3}(MgFe_{23}O_{4.1})_{0.37}) + 0.2CO_2$$

In fact, the results of the XRD patterns, N_2 isotherms, FTIR spectra, VRM, TGA, TEM and SEM/EDX analyses indicate the existence of Fe_3O_4 in the layered structure of Mg,Fe-LDHs of the obtained Mg,Fe-LDH·xFe_3O_4 ($0 < x < 1.0$) nanocomposites, thereby making them the most suitable materials for MSPE.

3.2. Adsorption performance for pharmaceuticals

To obtain magnetic nanocomposites with the appropriate adsorption performance toward target DCF molecules, several parameters were optimized including the pH of the medium, removal and equilibrium parameters. The Mg,Fe-LDHs and Mg,Fe-LDHs·0.3Fe_3O_4 samples were selected as the representative adsorbents because they demonstrate essentially different properties in the removal experiments.

3.2.1. Effect of the solution pH on DCF adsorption. The pH of the medium is one of the important influencing factors on the behavior of Fe_3O_4 nanoparticles and Mg,Fe-LDHs in solution.[43] Hence, the magnetic composites can exhibit excellent sensitivity to the pH of the medium. The pK_a of DCF is 4.21, and the carboxyl group of DCF was fully deprotonated at pH values higher than the pK_a values (Fig. S6, ESI†). Therefore, the effect of pH on the uptake of DCF by the obtained samples was studied by varying the pH value in the range of 5–11 (Fig. 7).

As presented in Fig. 7, it was found that the pH of the solution has a major effect on the adsorption capacity in the entire range of studied pH values. The Mg,Fe-LDHs do not exhibit an obvious adsorption when the pH value is below 6. This may be explained by the fact that the Mg,Fe-LDHs have positive charges below the pH_{PZC} (9.94, Fig. S7, ESI†), and efficient interaction occurs between DCF and the surface of

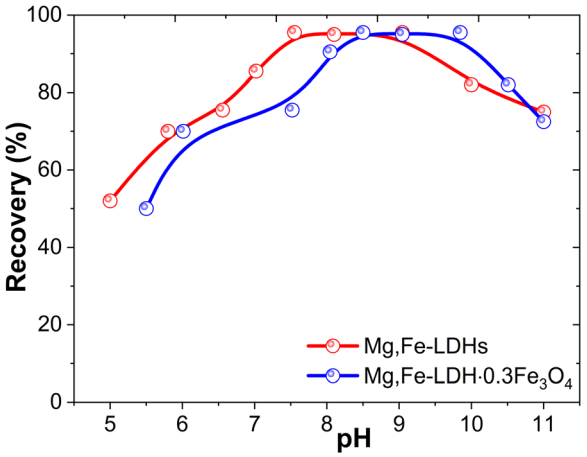

Fig. 7 Effect of the pH value on the recovery of DCF by the initial Mg,Fe-LDHs and Mg,Fe-LDH·0.3Fe_3O_4 (conditions: V = 200 mL, C = 500 ng mL^{-1} and weight 50 mg).

the brucite-like layer motifs. Thus, the surface of Mg,Fe-LDHs carries a positive charge below pH_{PZC}, facilitating the adsorption of DCF through electrostatic forces. Conversely, at pH values above the pH_{PZC}, the surface of Mg,Fe-LDHs becomes negatively charged. This may lead to electrostatic repulsion with DCF molecules, resulting in decreased adsorption capacity (Fig. 7). This further demonstrates the participation of electrostatic interactions in the adsorptive removal of DCF on the Mg,Fe-LDHs. This effect was also observed with a slight shift to basic pH for the magnetic nanocomposites. It has been shown that DCF was efficiently absorbed at pH 7.0–8.5 and 7.5–9.5 for the Mg,Fe-LDHs and Mg,Fe-LDH·0.3Fe_3O_4 samples. The high removal of DCF at pH (6.7–7.5) could be due to the hydrogen bonding formation and metal complexation. So, the DCF motifs mainly carboxylic-interact with the Fe(III) ions of the matrix, and form complexes based on coordination bonds.[25] The formation of the Fe(III)-ligand coordination bonds is based on the theory of "*hard and soft acids and bases*" (HSAB). The HSAB principle states that Fe(III) ions as hard Lewis acids prefer to combine with hard bases, such as water (donor atom, O) molecules and DCF (N,O donor atoms) anions to generate stable complexes. The surface complexes involve the bonding of several Lewis base species to one Lewis acid center.

Therefore, a pH value of 7.5–8.5 was chosen as an optimum value for subsequent experiments. The pH of environmental water is usually around 7.5–9.0; in this case, it is not necessary to adjust the solution pH for practical applications of the adsorbents.

3.2.2. The adsorbent hydrolytic stability. The hydrolytic stability of the adsorbents has been studied within a wide pH range from 5.0 to 10.0 (Fig. 8). The concentration of Mg^{2+} and Fe^{3+} ions in the solution remains constant for the samples treated with stress solution within the pH range of 7.0–9.4. This is fully consistent with the literature data for the hydrolytic stability of LDH-based adsorbents (*e.g.*, ref. 17).

According to AAS analysis, the maximum leaching amount of Fe^{3+} ions from Mg,Fe-LDHs at DCF sorption under the

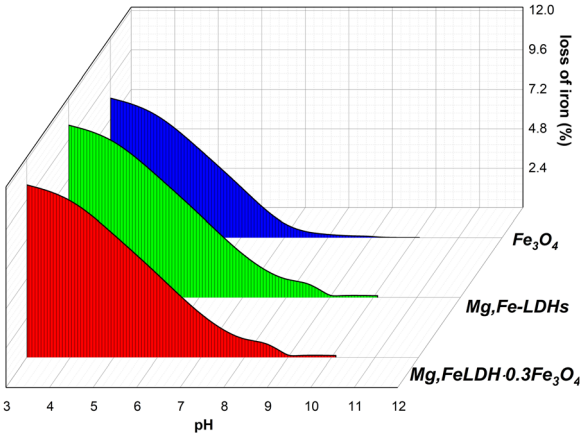

Fig. 8 Effect of the pH value on the stability of the obtained materials after 24 hours contact time.

studied pH solution was found to be 0.004 mg L^{-1} (0.1 g solid added to 50 mL solution). However, the maximum leaching of Mg^{2+} ions was found to be significant, indicating that the material may not be safe under all conditions.

3.2.3. Effect of sample volume. The effect of the sample volume was studied using different volumes of sample solution (20.0–200.0 mL) for a fixed quantity of obtained materials (Fig. 9a). The experimental results show that the removal percent decreased when the sample volume was greater than 250.0 mL. Therefore, the sample volume was set as 200.0 mL.

3.2.4. Effect of the amount of sorbent. The amount of sorbent plays a crucial role in the MSPE procedure (Fig. 9b). In the present study, the effect of the amount of Mg,Fe-LDH·$0.3Fe_3O_4$ is investigated by varying its loading in the range of 20–100 mg. When the amount of adsorbent is increased from 20 to 50 mg, the extraction efficiencies of the analyte increase correspondingly, which is explained by the higher quantity of active sites. However, the extraction capacities remain unchanged when the amount of adsorbent exceeds 50 mg, indicating the complete saturation of the Mg,Fe-LDH·$0.3Fe_3O_4$ active centers. Based on these results, it has been concluded that 50 mg is an optimal adsorbent loading amount for the extraction.

3.2.5. Effect of the magnetic separation time. To reach the equilibrium of magnetic separation procedure, the extraction time was investigated in the range of 5 to 60 s. The magnetic composites were completely separated after quantitative recoveries of the target metal ions when the magnetic field was applied for greater than 10 s. When the solution was higher than 50 mL, the separation time was longer than 30 s (for 400 mL). These results indicated that the developed MSPE procedure was very efficient and fast. In our experiments, a separation time of 10–30 s was employed depending on the volume solution. Specifically, 15 s was selected as the optimum extraction time.

Based on the above main properties of the obtained materials, the nanocomposites Mg,Fe-LDH·$0.3Fe_3O_4$ and Mg,Fe-LDH·$0.5Fe_3O_4$, which can form a stable colloidal suspension in aqueous solution and good extraction by NdFeB magnet, were chosen for studying the adsorption properties.

3.2.6. Adsorption kinetics. The influence of the contact time on DCF adsorption is shown in Fig. 10a. The adsorption capacities of the tested samples toward DCF increased quickly in the first 60 min, then gradually increased, and finally reached a stable plate. Adsorption equilibrium of the adsorbents was achieved after 2 hours, except for Fe_3O_4 (90 min). The adsorption kinetics of DCF to goethite also showed similar phenomena in a wide pH range.[25]

Pseudo-first order and pseudo-second order models were used to fit the adsorption kinetic data (Fig. 10b and c), and the parameters are summarized in Table 4. Correlation coefficients ($R^2 > 0.98$) of the pseudo-second order kinetic model obtained from the DCF adsorption were higher than that for the pseudo-first order kinetic model. When the second-order model is applied, the rate constant (k_2) varies from 1.2054 to 0.1842 g $mmol^{-1}$ min^{-1}. Moreover, the calculated adsorption capacities obtained from this kinetic model were approximately close to the experimental data. Therefore, the adsorption of DCF on the above materials could be dominated by the chemisorption process[44] with a rate-limiting step at all-time intervals. Similar results have been obtained for the adsorption of DCF by the Zn,Al-LDH·xBi_2O_3[20] and CS@PANI@Mg,Al-LDH[21] composites.

However, the removal of DCF on the obtained nanomaterials was not expected to only follow typical kinetic models, and a

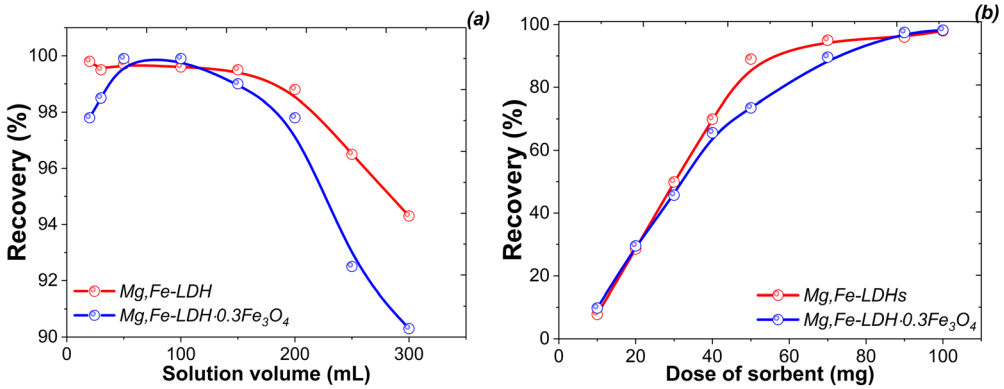

Fig. 9 Effect of the solution volume (a) and dose of the sorbent (b) on the DCF sorption by Mg,Fe-LDHs and Mg,Fe-LDH·$0.3Fe_3O_4$ samples.

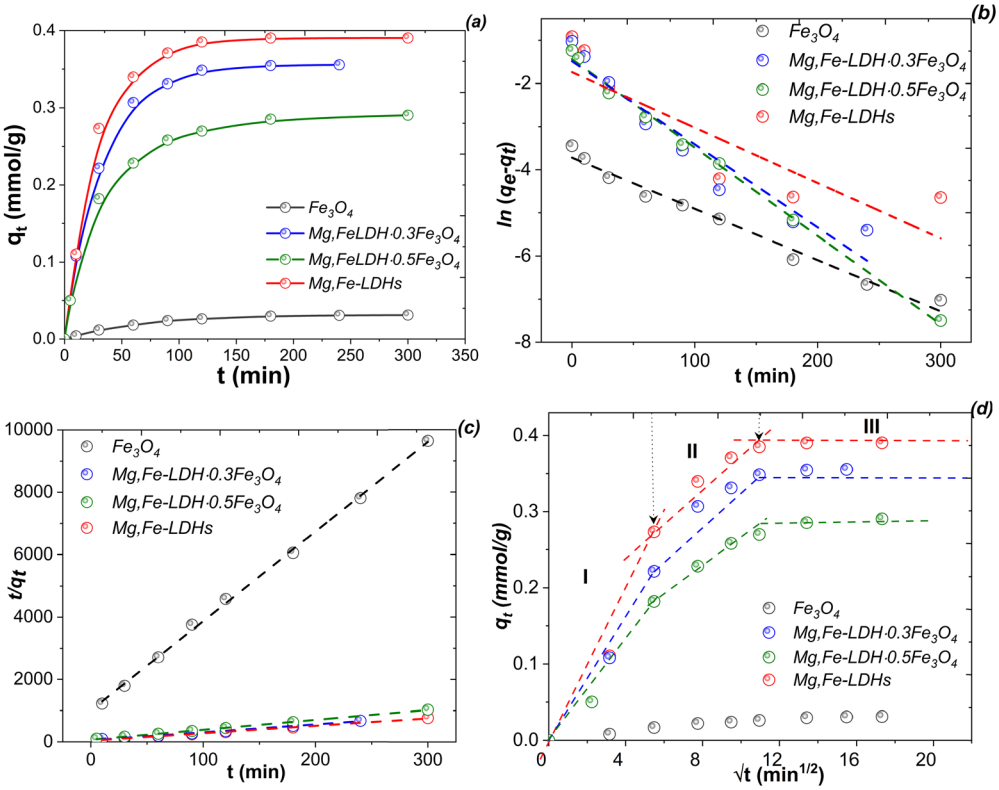

Fig. 10 Effect of the contact time on the DCF adsorption by Mg,Fe-LDHs and the corresponding magnetic materials (a), and the related data fitting by pseudo-first-order (b), pseudo-second-order (c), and Weber–Morris (d) models (conditions: C_0 = 300 mg L^{-1}, pH$_0$ = 7.5 ± 0.1, T = 25 °C, m/V = 1.0 g L^{-1}).

Table 4 Kinetic parameters of fitting with pseudo-first order and pseudo-second order models for DCF adsorption on Mg,Fe-LDHs and corresponding magnetic adsorbents at pH$_0$ = 7.5

Sample	q_e^{exp} (mmol g^{-1})	Pseudo-first order model			Pseudo-second order model		
		q_e^{cal} (mmol g^{-1})	k_1 (min^{-1})	R^2	q_e^{cal} (mmol g^{-1})	k_2 (g mmol^{-1} min^{-1})	R^2
Mg,Fe-LDHs	0.38	0.22	0.022	0.8612	0.42	0.1842	0.9919
Mg,Fe-LDH·0.3Fe_3O_4	0.37	0.23	0.019	0.9251	0.38	0.1868	0.9823
Mg,Fe-LDH·0.5Fe_3O_4	0.29	0.31	0.022	0.9012	0.31	0.2027	0.9946
Fe_3O_4	0.03	0.08	0.013	0.9529	0.03	1.2051	0.9898

q_e^{exp} and q_e^{cal} are the experimental and calculated adsorption capacity at equilibrium, respectively (mmol g^{-1}); k_1 and k_2 are the pseudo-first-order and pseudo-second-order rate constants, respectively.

number of other mechanisms might be governing the adsorption processes. In this context, to demonstrate the molecular diffusion effect, the Weber–Morris (or intra-particles diffusion) kinetic model[45] is applied. The plots and values of the corresponding rate constants are presented in Fig. 10d and Table S1 (ESI†), respectively. In Fig. 10d, the graphs do not have a linear fitting plot, indicating that the removal process was controlled by several factors. The fitting plots contain three different regions, which is consistent with various step adsorption processes. The first stage involves rapid adsorption (~75%) on the surface of the materials within a period of the initial 60 min. The rate constant (K_i) is larger in the obtained magnetic nanocomposites than the pristine Mg,Fe-LDHs due to the large specific surface area (Table 2). The second stage involves a decrease in the slope of the fitting line, suggesting a reduction in the adsorption sites of the adsorbents as they are consumed, resulting in a decrease in the adsorption rate. This effect also suggests that the process is primarily adsorption in the exterior surface, along with some absorption inside the interlayer space. In the third stage, the slope of the fitting line is nearly zero, indicating a lack of adsorption sites, and the adsorption process reaches the equilibrium state.

The intercept (C) values of the obtained adsorbents are observed between 0.0005 mmol g^{-1} (I stage) and 0.3781 mmol g^{-1} (III stage) (Table S1, ESI†). It is known[45] that with a greater value of C, there is a greater boundary layer effect in the sorption process. In this case, the effect of the boundary layer thickness is very important for the sorption in the III stage compared to

the sorption in the I stage. This observation also indicates that the intra-particles diffusion of the DCF species is not the dominating factor controlling the mechanism of the adsorption process.

3.2.7. Adsorption isotherms. Through adsorption isotherms, the equilibrium relationship between the adsorbate and adsorbents was analyzed. Fig. 11 and Fig. S8 (ESI†) present the adsorption isotherms of DCF onto the as-synthesized samples. The adsorption process on Mg,Fe-LDHs and Mg,Fe-LDH·xFe$_3$O$_4$ samples exhibits an L-type isotherm.[46] This indicates that DCF is strongly attracted with the adsorbents, mostly by chemisorption between cations in the brucite-like layer and DCF groups, which suggests that the layer charge may be important. The obtained experimental isotherms (Fig. 11) illustrate the quantitative removal of DCF onto the obtained materials at low concentrations. Then, the sorption of DCF onto the obtained materials was gradually improved, and finally attained the platform. The slope of the isotherm inclination indicates the affinity of the adsorbent to the adsorbate.[46] Meanwhile, it was observed that the adsorption affinities of all the obtained samples differed. In this key, the pristine Mg,Fe-LDHs have the highest affinity to the DCF ions, and quantitatively adsorb them from the water solution up to the total capacity of the adsorbent. With increasing Fe$_3$O$_4$ amount, the adsorption capacity of the magnetic nanocomposites decreased, which may be attributed to the blocked active spaces. This is because the loading of Fe$_3$O$_4$ results in two opposite effects. It decreases the number of adsorption sites, thereby enhancing the magnetic properties. It also enhances the extent of aggregation, thereby limiting the availability of active sites. At low concentrations, the magnetic material has sufficient active sites for the analyte to be completely adsorbed, but the adsorbed amount per unit mass can be relatively weak. At higher concentrations, the increase in concentration improves the adsorptive capacity of mass transfer, and thus the adsorptive capacity per unit weight becomes larger. However, due to the limited number of active sites on the surface of the magnetic nanocomposites, the adsorption will be in equilibrium as the concentration is further increased, resulting in a gradual decrease in the removal efficiency.

The experimental adsorption capacities toward DCF for the Mg,Fe-LDHs, Mg,Fe-LDH·0.1Fe$_3$O$_4$, Mg,Fe-LDH·0.3Fe$_3$O$_4$, Mg,Fe-LDH·0.5Fe$_3$O$_4$ and Mg,Fe-LDH·1.0Fe$_3$O$_4$ samples were 158.1 mg g^{-1} (0.49 mmol g^{-1}), 153.2 mg g^{-1} (0.48 mmol g^{-1}), 143.2 mg g^{-1} (0.45 mmol g^{-1}), 124.3 mg g^{-1} (0.38 mmol g^{-1}), and 89.1 mg g^{-1} (0.28 mmol g^{-1}), respectively (Fig. 11 and Fig. S8, ESI†). The starting Mg,Fe-LDHs exhibit the highest adsorption performance due to the positive charge on the surface, and resulting in electrostatic repulsions between the DCF ions and Mg,Fe-LDHs. With increasing Fe$_3$O$_4$ amount, the adsorption capacity of the magnetic nanocomposites decreased, which may be attributed to the Mg,Fe-LDHs being stacked randomly on the surface of Fe$_3$O$_4$ and blocking the interlayer. This is not beneficial for removing DCF motifs in the magnetic solid-phase extraction process from aqueous solution.

The isotherm models are a serious justification for evaluating the interaction between the organic molecules on the surface adsorbents and DCF in the solution at the equilibrium state.[10,21] To further understand the adsorption mechanism of DCF by adsorbents, we used four classic adsorption model fits, Langmuir, Freundlich, Temkin and Redlich–Peterson. The Langmuir model represents a uniform surface property of the adsorbent, where only one molecule can be adsorbed at each adsorption site. The Freundlich model represents a non-uniform surface property, where a multimolecular overlay can be formed on the adsorption sites. The Redlich and Peterson model[47] describes the low and high concentration limits of the Langmuir and Freundlich equations. The fitting curves of the isotherm adsorption models of the obtained adsorbents for DCF removal are plotted in Fig. S9 (ESI†) with the parameters shown in Table 5.

The Langmuir isotherm equation ($R^2 \geq 0.9940$) displayed a better goodness of fit than the other tested equations, suggesting monolayer adsorption, and the calculated capacity (q_m, Table 5) values of the obtained adsorbents from the Langmuir equation is very close to the values of the equilibrium experimental quantity adsorbed, as shown in Fig. 11. The K_L values for DCF adsorption on the above adsorbents were all between 0 and 1, thereby confirming the dominant chemisorption process. According to the Freundlich equation at constant system pH, the adsorption isotherms of DCF on solids exhibited a nonlinear characteristic ($1/n < 1$), and also indicated a minimum interaction between the adsorbed DCF motifs. The nonlinearity of the sorption behaviors indicated specific interactions with functional groups on the obtained sorbents. Due to the low correlation coefficients ($R^2 \geq 0.7546$), the Freundlich equation was mainly ignored. The Temkin isotherm equation indicates the chemisorption process because the b_t value was higher than 20 kJ mol^{-1}.[48] The linear fitting of the equilibrium data indicated that the experimental adsorption isotherm obtained for Mg,Fe-LDH 0.5Fe$_3$O$_4$ was best fitted to the Redlich–Peterson model, with the highest R^2 parameter (shown in Table 5).

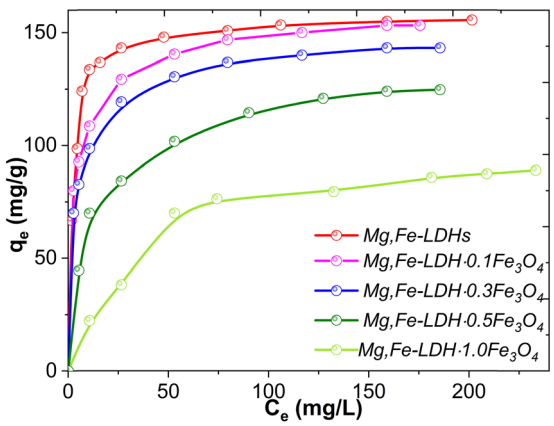

Fig. 11 Adsorption isotherms of DCF onto Mg,Fe-LDHs and the corresponding magnetic nanocomposites at room temperature (conditions: pH = 7.5 ± 0.1, m/V = 1.00 g L^{-1}, time = overnight).

Table 5 Parameters of four kinds of isotherm adsorption models for DCF adsorbed onto the obtained adsorbents at pH_0 = 7.5

Model	Parameter	Mg,Fe-LDHs	Mg,Fe-LDH·0.1Fe_3O_4	Mg,Fe-LDH·0.3Fe_3O_4	Mg,Fe-LDH·0.5Fe_3O_4	Mg,Fe-LDH·1.0Fe_3O_4	Fe_3O_4
Langmuir	K_L, (L mg^{-1})	0.42	0.22	0.2	0.08	0.03	0.09
	q_m, (mg g^{-1})	156.25	156.24	147.06	133.33	102.04	30.4
	R^2	0.9999	0.9997	0.9997	0.9997	0.9989	0.994
Freundlich	K_F, ($mg^{1-1/n}$ $L^{1/n}$ g^{-1})	81.4	72.88	63.61	33.08	9.6	7.41
	$1/n$	0.14	0.15	0.17	0.27	0.43	0.29
	R^2	0.7546	0.9644	0.9598	0.9449	0.8971	0.9532
Temkin	A_T (L mg^{-1})	154.04	37.82	22.4	1.74	1.61	1.52
	b_t, (J mol^{-1})	153.84	138.07	138.94	111.67	112.84	453.01
	R^2	0.832	0.9838	0.9822	0.988	0.9424	0.9838
Redlich–Peterson	K_{RP} (L mg^{-1})	3.65	7.13	0.40	0.19	0.16	0.14
	a_{RP} (L mg^{-1})$^{\beta}$	0.41	0.49	0.12	0.22	0.13	0.67
	β	0.75	0.76	0.29	0.17	0.48	0.52
	R^2	0.9579	0.9690	0.9998	0.9899	0.9999	0.9888

q_m and K_L are the Langmuir constants related to the capacity of adsorbents and energy of adsorption, respectively; K_F is the partitioning Freundlich coefficient, and $1/n$ is the dimensionless reaction order (commonly less than 1); b_t is the Temkin constant related to the heat of sorption, A_T is the equilibrium binding constant corresponding to the maximum binding energy; K_{RP} is the Redlich–Peterson adsorption capacity constant; a_{RP} is the Redlich–Peterson isotherm constant; and β is an exponent (dimensionless) between 0 and 1.

Table 6 Comparison of the sorption properties of the prepared composites toward DCF with some LDH-based reported sorbents

No.	Sorbent	Adsorption performance (q_m, mg g^{-1}; time, min; pH medium, *etc.*)	Ref.
Pristine LDHs materials			
1	Zn,Fe-LDH	74.5 mg g^{-1}; time 30 min, the pseudo-second order kinetic model.	18
2	MgAl-LDH (or calcined at 500 °C)	123 mg g^{-1} (or 1494 mg g^{-1})	19
3	MgAl-LDH	104 mg g^{-1}; m/V = 5/20 mg mL^{-1}	22
4	Zn,Al-LDH (or calcined at 500 °C)	94.32 mg g^{-1} (737.02 mg g^{-1}), t = 20 min, the pseudo-second order kinetic model; pH = 7.0, V = 50 mL, m = 50 mg, T = 22 °C.	24
5	(Co, Mg, Ni and Zn),Al-LDHs	38 mg g^{-1}, 78 mg g^{-1}, 16 mg g^{-1} and 150 mg g^{-1}; 0.1–0.4 mg L^{-1}, 298 K, pH 6; pseudo-second order linear reaction.	26
6	Mg,Fe-LDHs	158.1 mg g^{-1}, pH = 7.5, Langmuir isotherm model, suggesting the chemisorption process.	This study
LDHs-based composites			
7	Zn,Al-LDH·$x$$Bi_2O_3$	500 mg g^{-1} (Zn,Al-LDH·1.0Bi_2O_3);	20
8	CS@PANI@Mg,Al-LDH	618.16 mg g^{-1}, pH = 5.5 ± 0.1, m/V = 0.5 g L^{-1}; t = 2–4 h, the pseudo-second order kinetic model; Langmuir isotherm model, suggesting the monolayer adsorption.	21
9	MgAl-LDH/PmPD	588 mg g^{-1}, K_d = 1.3 × 10^4 mL g^{-1}, time 2 h, pseudo-second order kinetic model.	22
10	Cellulose acetate/Mg–Al-LDH	pH = 7, the CA membrane retained only 2.7% of the drug due to a lack of electrostatic interaction between the neutral polymer and the negatively charged DCF molecule.	23
11	Fe_3O_4/cellulose/ionomer/CaAl–LDHs	258 mg g^{-1}, t = 2 min, Langmuir model (at low concentration) and Freundlich model (at high concentration level).	35
12	Mg,Fe-LDH·$x$$Fe_3O_4$ (x = 0.1, 0.3, 0.5, 1.0 and 2.0)	153.2 mg g^{-1} (0.48 mmol g^{-1}), 143.2 mg g^{-1} (0.45 mmol g^{-1}), 124.3 mg g^{-1} (0.38 mmol g^{-1}), 89.1 mg g^{-1} (0.28 mmol g^{-1}) and 76.1 mg g^{-1} (0.23 mmol g^{-1}); m/V = 1.0 g L^{-1}; pH = 7.5, Langmuir isotherm model, suggesting the chemisorption process.	This study

Notes. CS – carbon sphere; PmPD – Poly(*m*-phenylenediamine).

3.2.8. Comparison of the adsorption capacities. The adsorption capacities of the obtained materials and other adsorbents reported in the literature for DCF are shown in Table 6.

At pH_0 of 7.5, the maximum adsorption capacity of the starting Mg,Fe-LDHs towards DCF is 158.1 mg g^{-1}, and this capacity can be much higher than those reported in other works for pristine LDHs (Table 6). This outcome was ascribed to the fact that the specific reaction (*e.g.*, complex-formation) of the brucite-like structure of Mg,Fe-LDHs with DCF took place during the adsorption process. It is obvious that the performances of the prepared nanocomposites are at a satisfactory level with respect to the adsorption capacity among the reported LDHs-based hybrid materials. Thus, these prepared materials could be well suited for practical applications.

3.3. Adsorption mechanisms

To elucidate the interaction mechanisms between DCF and Mg,Fe-LDHs (or magnetic Mg,Fe-LDH·0.3Fe_3O_4), XRD and FTIR analyses were conducted, as shown in Fig. 12.

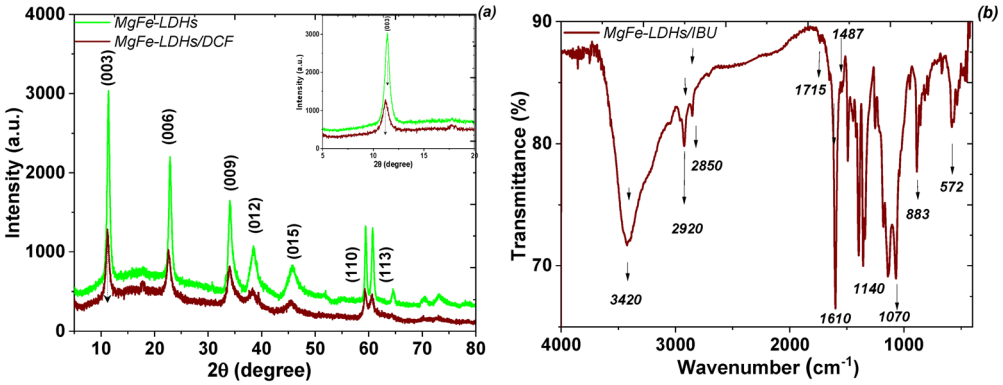

Fig. 12 XRD patterns (a) and FTIR spectra (b) of Mg,Fe-LDHs before and after adsorption of DCF ions.

By comparison of the XRD patterns before and after the adsorption of DCF (Fig. 12a), we can see that some diffraction-angle peaks are decreased (11.40° to 11.24°, 22.95° to 22.63°) and some peaks are increased (56.67° to 59.92°), while other peaks remained unchanged. The diffraction angle at 39.4588° in the XRD pattern after adsorption belongs to DCF. The basal peak (2θ = 36.2169°) position in the drug-containing product (Mg,Fe-LDHs/DCF, Fig. 12a) corresponds to an interlayer layer distance of 7.8598 Å, which is slightly higher than that of Mg,Fe-LDH by 0.00917. This means that the diclofenac ions mainly are not intercalated in the interlayer space of the layered structure. The 2θ values of the highly intense peaks for the initial Mg,Fe-LDHs and Mg,Fe-LDHs/DCF products are 36.3559° and 36.2169°, respectively. This effect is probably due to the interactions of the organic groups with the surface of the material and complexation of the layer-formed metal cations (Mg(II) and Fe(III)) of the Mg,Fe-LDHs plates. The results obtained from XRD analysis are consistent with the previously reported data.[18]

The FTIR spectra of Mg,Fe-LDHs before and after DCF adsorption were also recorded (Fig. 12b). Generally, the spectrum of DCF exhibited typical peaks at 3380 cm^{-1}, 3030 cm^{-1}, 1585 cm^{-1}, 1556 cm^{-1}, 1451 cm^{-1}, 1289 cm^{-1}, ν(C–N_{Ar}), and 750 cm^{-1} due to the ν(N–H), ν(C–H_{Ar}), δ(C=C_{Ar}), δ(N–H), $\nu(COO^{-})$ and ν(C–Cl) stretching vibrations, respectively. After DCF sorption, the peaks corresponding to ν(N–H), ν(COO), and ν(C–Cl) were shifted. This change indicated the existence of a chemical interaction between DCF and Mg,Fe-LDHs. Complexation between the =N–H and –COOH groups of DCF and the metal ions of the brucite-like layers may have occurred.[25] Additionally, the wide peak of the ν(O–H) stretching vibration of Mg,Fe-LDHs near 3440 cm^{-1} was shifted to 3396 cm^{-1}, which was probably attributed to the formation of N···O and O···HO hydrogen bonding between DCF and the brucite-like layers of the Mg,Fe-LDHs plates. Based on the FTIR data of Mg,Fe-LDHs before and after adsorption, the uptake mechanism could be explained *via* electrostatic interaction, hydrogen bonding, and complexation interactions (Scheme 2). Moreover, adsorption takes place at the surface of the magnetic nanocomposites through electrostatic forces of attraction for DCF, accompanied by intercalation of CO_3^{2-} anions from aqueous solution, which consequently remained unchanged by DCF *via* anion exchange according to XRD data.

3.4. Regeneration of the adsorbents

Reusability is one of the key factors for evaluating the economic viability of novel sorbents. For this purpose, the

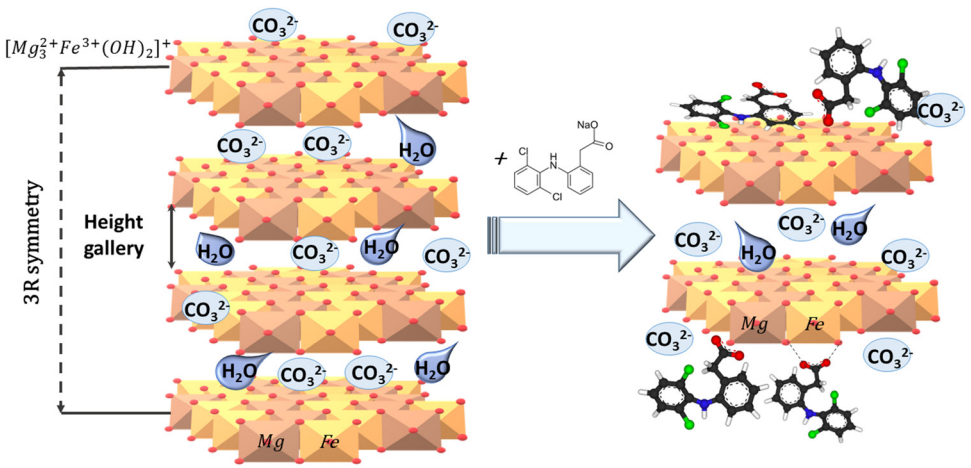

Scheme 2 Schematic presentation of the adsorption mechanisms of DCF onto Mg,Fe-LDHs (or Mg,Fe-LDH·xFe_3O_4) samples.

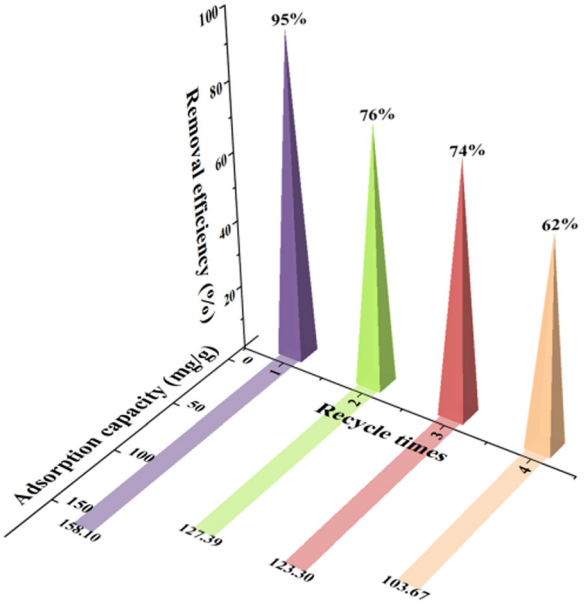

Fig. 13 Reusability of the Mg,Fe-LDH·0.3Fe_3O_4 sample for the adsorption/desorption of DCF in aqueous solution.

Mg,Fe-LDH·0.3Fe_3O_4 nanocomposite was selected as a model sample. The adsorption capacity of the Mg,Fe-LDH·0.3Fe_3O_4 magnetic nanocomposite for three consecutive adsorption–desorption cycles is presented in Fig. 13. The regeneration studies for the nanocomposite reveal that 69–79% of the adsorbed analytes can be removed by washing (within 300 min) the DCF-adsorbed nanocomposites once with Na_2CO_3 (or $NaNO_3$) solution. During the adsorption/desorption process, the non-renewable nature of the complexation reaction is the main reason for the gradual decrease in the removal of DCF ions. Thus, upon several repeated inorganic salts-treatment processes, the exhausted magnetic adsorbents can be regenerated.

3.5. Multicomponent model solution study

Under real conditions, the effective removal of a pollutant from the water matrix is significantly affected by the presence of other components with various concentrations.[1,6] To conduct the selectivity study of the proposed magnetic adsorbents, the effect of interfering ions on the adsorption process was characterized using a multicomponent model solution (simulated water). Under the optimized experimental conditions, the effects of both cations (multi element ICP standard solution contains 23 elements) and anions (Cl^-, NO_3^- HPO_4^{3-}, SO_4^{2-} and humic acids (A–)) on the adsorption of DCF were investigated. In this sense, various coexisting ions (approximately 4 mg L^{-1} of each component) were added to 50 mL aqueous solutions containing DCF with a concentration of 10 mg L^{-1} (Fig. 14).

The mono- and doubly-charged cations showed different effects of the removal of DCF motifs on the adsorbents (Fig. 14a). Among them, Na^+ and K^+ ions only showed a minor influence on the adsorption of DCF. Alkaline earth metals (especially Ca^{2+} ions) were shown to have a relatively significant effect. Pb^{2+}, Ni^{2+}, Co^{2+} and other double-charged ions will cause interference if its concentration is more than 10 times over the DCF solution (Fig. 14a). Generally, double-charged cations had a greater influence than monocharged cations. Although the divalent cations showed insignificant effects on the adsorption of the target analyte, AAS showed that the concentration of Mg(II) ions in solution was significantly increased after the adsorption procedure. The mechanisms of these doubly-charged cations affecting the adsorption process would be integrated, including the effect of ionic strength, the effect of competitive adsorption, and the effect of isomorphic substitution with matrix Mg(II) ions. From Fig. 14b, it can be observed that the potentially interfering anions have no significant effect on the removal of DCF by the proposed procedure using the Mg,Fe-LDH·0.3Fe_3O_4 sample. A slight reduction in the sorption of DCF can be observed in the presence of Cl^- and NO_3^-, and the interference effect was much stronger in the presence of humic acid.

To demonstrate the applicability of the developed procedure for real-time wastewater treatment, tests were performed at high concentrations of co-existing ions. In this case, the tolerance limit was taken as the concentration of the co-existing ions causing a variation in the intensity of DCF within ±25%. The tolerable ratio of each species concentration was as follows:

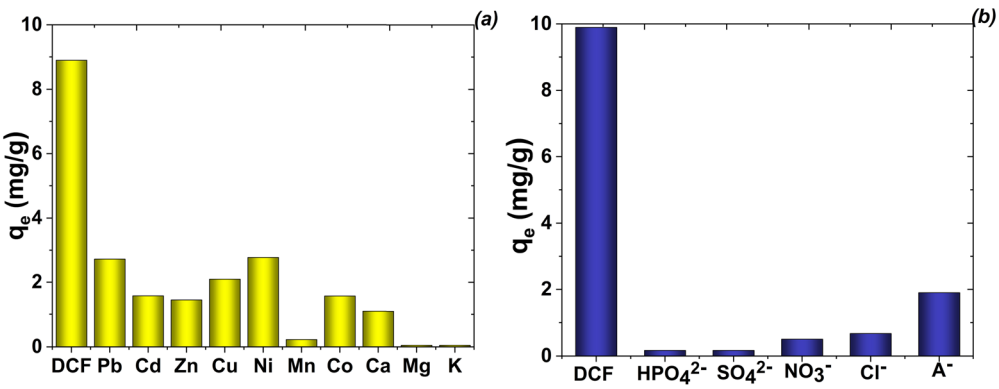

Fig. 14 Effect of the coexisting cations (a) and anions (b) on the DCF removal in multi-component solutions by the Mg,Fe-LDH·0.3Fe_3O_4 sample (conditions: C(DCF) = 10 mg L^{-1}, C(M) = C(A^-) = 4 mg L^{-1}, time 300 min, m/V = 1.0 g L^{-1}, pH 7.5).

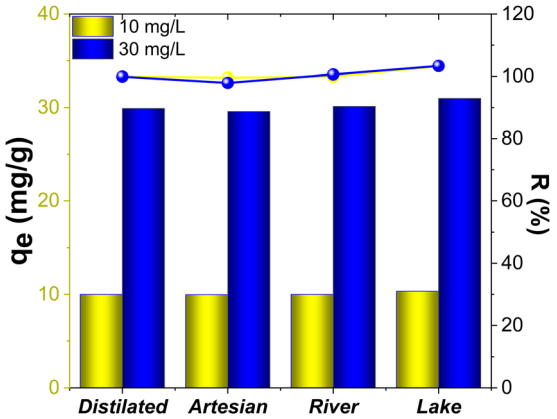

Fig. 15 Analytical results and recovery of DCF on Mg,Fe-LDH·0.3Fe_3O_4 in various real samples under the optimum conditions.

1000-fold for K^+ and Na^+ (from their nitrate salts); 10-fold for Pb^{2+}, Cu^{2+}, Cd^{2+}, Zn^{2+}, Al^{3+}, Mn^{2+}, Ni^{2+}, and Co^{2+} (from their nitrate salts); and 20-fold for Mg^{2+} and Ca^{2+} (from their nitrate salts); 100-fold for PO_4^{3-}, Cl^-, NO_3^- and SO_4^{2-} (from their sodium salts) ions.

3.6. Application to real water samples

The adsorption potential of the magnetic nanocomposites was explored *via* the removal of DCF in three real samples (artesian water, river water, and lake water (near pharmaceutical manufacturing plant)) by adding the samples with various DCF concentrations. The adsorption capacity data and the recoveries for spiked samples are shown (Fig. 15).

As illustrated in Fig. 15, DCF was removed entirely from all studied water samples. The average values of recovery on the spiked DCF in different samples ranged from 98.5% to 103.3%.

The good magnetic and adsorptive parameters of the obtained materials indicate that the proposed procedure has potential for MSPE of other pharmaceuticals from aqueous solution. As a result, the as-synthesized composites appear to be a promising platform for the removal of emerging organic pollutants from water media, and mainly without the use of an anion exchanger.

4. Conclusions

In summary, the Mg,Fe-LDH·$x$$Fe_3O_4$ (x = 0.1, 0.3, 0.5, 1.0 and 2.0) nanocomposites as an efficient sorbent were synthesized *via* sonification treatment of both components. The molar ratio of Mg,Fe-LDHs/Fe_3O_4 had a significant effect on the 2D-layered structure and specific surface area of the magnetic nanocomposites. The Mg,Fe-LDH·$x$$Fe_3O_4$ samples with $0.1 \leq x \leq 1.0$ have a high magnetic saturation, and are well suited for magnetic solid phase extraction of pharmaceuticals from aqueous solution. High adsorption capacities of magnetic nanocomposites were obtained toward diclofenac sodium as a model pharmaceutical. The optimum pH for the removal of diclofenac by magnetic nanocomposites is about 7.5. The removal effectivity of diclofenac anions by Mg,Fe-LDH·$x$$Fe_3O_4$ samples decreases with increasing Fe_3O_4-loading on the chemical composition of adsorbents. Analyte adsorption of the obtained nanocomposites is described by the Langmuir adsorption isotherm model, suggesting the monolayer adsorption process, whereas the Weber–Morys model indicates that the adsorption of diclofenac mainly occurs on the external surface. Conversely, the adsorption kinetic data for pollutants were well fitted to the pseudo-second-order model. Simultaneously, based on the XRD and FTIR data of samples before and after adsorption, the removal mechanism could be explained through electrostatic interaction (including hydrogen bonding) between adsorbents and diclofenac motifs, and complexation reactions in a heterogeneous system. With the overcoming of certain limitations related to the chemical composition of nanocomposites and excess double-charged inorganic cations in solution, they are poised to become a ubiquitous tool for environmental remediation efforts.

Author contributions

Tetiana Hubetska: investigation, visualization, formal analysis, software; Victor Demchenko: formal analysis, investigation, data curation; Natalia Kobylinska – investigation, original draft, conceptualization. All authors have read and agreed to the published version of the manuscript.

Data availability

ESI,† is available in the additional files, and further supporting data are available from the authors on request.

Conflicts of interest

There are no conflicts to declare.

Acknowledgements

The authors gratefully acknowledge the support of MINECO (Spain) for MCI-21-PID2020-113558RB-C41 and PID2020-119130 GB-I00 grants, providing materials characterization facilities. Dr Natalia Kobylinska would like to thank the European Chemistry School for Ukrainians.

References

1 P. Sathishkumar, R. A. A. Meena, T. Palanisami, V. Ashokkumar, T. Palvannan and F. L. Gu, Occurrence, interactive effects and ecological risk of diclofenac in environmental compartments and biota – a review, *Sci. Total Environ.*, 2020, **698**, 134057, DOI: 10.1016/j.scitotenv.2019.134057.

2 S. Schmidt, H. Hoffmann, L. A. Garbe and R. J. Schneider, Liquid chromatography–tandem mass spectrometry detection of diclofenac and related compounds in water samples,

J. Chromatogr. A, 2018, **1538**, 112–116, DOI: 10.1016/j.chroma.2018.01.037.

3 M. Patel, R. Kumar, K. Kishor, T. Mlsna, C. U. Pittman and D. Mohan, Pharmaceuticals of emerging concern in aquatic systems: chemistry, occurrence, effects, and removal methods, *Chem. Rev.*, 2019, **119**, 3510–3673, DOI: 10.1021/acs.chemrev.8b00299.

4 M. O. Barbosa, N. F. F. Moreira, A. R. Ribeiro, M. F. R. Pereira and A. M. T. Silva, Occurrence and removal of organic micropollutants: an overview of the watch list of EU Decision 2015/495, *Water Res.*, 2016, **94**, 257–279, DOI: 10.1016/j.watres.2016.02.047.

5 J. Schwaiger, H. Ferling, U. Mallow, H. Wintermayr and R. D. Negele, Toxic effects of the non-steroidal anti-inflammatory drug diclofenac. Part I: histopathological alterations and bioaccumulation in rainbow trout, *Aquat. Toxicol.*, 2004, **68**, 141–150, DOI: 10.1016/j.aquatox.2004.03.014.

6 A. Jakimska, A. Kot-Wasik and J. Namieśnik, The Current State-of-the-Art in the Determination of Pharmaceutical Residues in Environmental Matrices Using Hyphenated Techniques, *Crit. Rev. Anal. Chem.*, 2014, **44**, 277–298, DOI: 10.1080/10408347.2013.835244.

7 D. I. de Souza, A. Giacobbo, E. da, S. Fernandes, M. A. S. Rodrigues, M. N. de Pinho and A. M. Bernardes, Experimental design as a tool for optimizing and predicting the nanofiltration performance by treating antibiotic-containing wastewater, *Membranes*, 2020, **10**, 1–15, DOI: 10.3390/membranes10070156.

8 F. Méndez-Arriaga, S. Esplugas and J. Giménez, Degradation of the emerging contaminant ibuprofen in water by photo-Fenton, *Water Res.*, 2010, **44**, 589–595, DOI: 10.1016/j.watres.2009.07.009.

9 H. Wang, S. Wang, Y. Liu, Y. Fu, P. Wu and G. Zhou, Degradation of diclofenac by Fe(II)-activated bisulfite: kinetics, mechanism and transformation products, *Chemosphere*, 2019, **237**, 124518, DOI: 10.1016/j.chemosphere.2019.124518.

10 M. S. Shamsudin, S. F. Azha and S. Ismail, A review of diclofenac occurrences, toxicology, and potential adsorption of clay-based materials with surfactant modifier, *J. Environ. Chem. Eng.*, 2022, **10**, 107541, DOI: 10.1016/j.jece.2022.107541.

11 F. Poorsharbaf Ghavi, F. Raouf and A. Dadvand Koohi, A Review on Diclofenac Removal from Aqueous Solution, Emphasizing on Adsorption Method, *Iran. J. Chem. Chem. Eng.*, 2020, **39**, 141–154.

12 T. S. Hubetska, A. S. Mestre, N. G. Kobylinska and A. P. Carvalho, Steam Activation of Acid-Chars for Enhanced Textural Properties and Pharmaceuticals Removal, *Nanomaterials*, 2022, **12**, 3480, DOI: 10.3390/nano12193480.

13 F. Cavani, F. Trifirb and A. Vaccari, Hydrotalcite-type anionic clays: preparation, properties and applications, *Catal. Today*, 1991, **11**, 173–301, DOI: 10.1016/0920-5861(91)80068-K.

14 L. Zhou, J. Liu, A. Lu, J. Shen, J. Xu and H. Jiang, Controllable synthesis of cubic magnetic $MgFe_2O_4$ derived from MgFe-LDHs for efficient removal of methyl orange, *Chem. Eng. J.*, 2022, **428**, 131174, DOI: 10.1016/j.cej.2021.131174.

15 A. F. da Silva, J. L. da, S. Duarte and L. Meili, Different routes for MgFe/LDH synthesis and application to remove pollutants of emerging concern, *Sep. Purif. Technol.*, 2021, **264**, 118353, DOI: 10.1016/j.seppur.2021.118353.

16 V. Rives, M. del Arco and C. Martín, Intercalation of drugs in layered double hydroxides and their controlled release: a review, *Appl. Clay Sci.*, 2014, **88–89**, 239–269, DOI: 10.1016/j.clay.2013.12.002.

17 J. W. Boclair and P. S. Braterman, Layered double hydroxide stability. 1. Relative stabilities of layered double hydroxides and their simple counterparts, *Chem. Mater.*, 1999, **11**, 298–302, DOI: 10.1021/cm980523u.

18 H. A. Younes, R. Khaled, H. M. Mahmoud, H. F. Nassar, M. M. Abdelrahman, F. I. Abo El-Ela and M. Taha, Computational and experimental studies on the efficient removal of diclofenac from water using ZnFe-layered double hydroxide as an environmentally benign absorbent, *J. Taiwan Inst. Chem. Eng.*, 2019, **102**, 297–311, DOI: 10.1016/j.jtice.2019.06.018.

19 B. A. Jimenez-López, R. Leyva-Ramos, E. Mendoza-Mendoza, D. E. Villela-Martínez and D. H. Carrales-Alvarado, Adsorption of diclofenac from water solution on layered double hydroxide Mg/Al/CO_3 synthesized from sulphate salts and calcined, *Environ. Nanotechnol., Monit. Manage.*, 2023, **20**, 100782, DOI: 10.1016/j.enmm.2023.100782.

20 P. Kumari, B. Pal and R. K. Das, Superior adsorptive removal of eco-toxic drug diclofenac sodium by Zn–Al LDH·$x$$Bi_2O_3$ layer double hydroxide composites, *Appl. Clay Sci.*, 2021, **208**, 106119, DOI: 10.1016/j.clay.2021.106119.

21 H. Xu, S. Zhu, M. Xia and F. Wang, Rapid and efficient removal of diclofenac sodium from aqueous solution via ternary core-shell CS@PANI@LDH composite: experimental and adsorption mechanism study, *J. Hazard. Mater.*, 2021, **402**, 123815, DOI: 10.1016/j.jhazmat.2020.123815.

22 T. Xiong, X. Yuan, H. Wang, Z. Wu, L. Jiang, L. Leng, K. Xi, X. Cao and G. Zeng, Highly efficient removal of diclofenac sodium from medical wastewater by Mg/Al layered double hydroxide-poly(*m*-phenylenediamine) composite, *Chem. Eng. J.*, 2019, **366**, 83–91, DOI: 10.1016/j.cej.2019.02.069.

23 M. D. Raicopol, C. Andronescu, S. I. Voicu, E. Vasile and A. M. Pandele, Cellulose acetate/layered double hydroxide adsorptive membranes for efficient removal of pharmaceutical environmental contaminants, *Carbohydr. Polym.*, 2019, **214**, 204–212, DOI: 10.1016/j.carbpol.2019.03.042.

24 N. Boukhalfa, M. Boutahala and N. Djebri, Synthesis and characterization of ZnAl-layered double hydroxide and organo-K10 montmorillonite for the removal of diclofenac from aqueous solution, *Adsorpt. Sci. Technol.*, 2017, **35**, 20–36, DOI: 10.1177/0263617416666548.

25 Y. Zhao, F. Liu and X. Qin, Adsorption of diclofenac onto goethite: adsorption kinetics and effects of pH, *Chemosphere*, 2017, **180**, 373–378, DOI: 10.1016/j.chemosphere.2017.04.007.

26 L. Santamaría, F. Devred, E. M. Gaigneaux, M. A. Vicente, S. A. Korili and A. Gil, Effect of the surface properties of Me^{2+}/Al layered double hydroxides synthesized from aluminum saline slag wastes on the adsorption removal of drugs,

Microporous Mesoporous Mater., 2020, **309**, 110560, DOI: 10.1016/j.micromeso.2020.110560.

27 M. Sajid and I. Ihsanullah, Magnetic layered double hydroxide-based composites as sustainable adsorbent materials for water treatment applications: progress, challenges, and outlook, *Sci. Total Environ.*, 2023, **880**, 163299, DOI: 10.1016/j.scitotenv.2023.163299.

28 R. Ran Shan, L. Guo Yan, K. Yang, Y. Feng Hao and B. Du, Adsorption of Cd(II) by Mg–Al–CO_3- and magnetic Fe_3O_4/Mg–Al–CO_3-layered double hydroxides: kinetic, isothermal, thermodynamic and mechanistic studies, *J. Hazard. Mater.*, 2015, **299**, 42–49, DOI: 10.1016/j.jhazmat.2015.06.003.

29 H. Zhang, G. Zhang, X. Bi and X. Chen, Facile assembly of a hierarchical core@shell Fe_3O_4@CuMgAl-LDH (layered double hydroxide) magnetic nanocatalyst for the hydroxylation of phenol, *J. Mater. Chem. A*, 2013, **1**, 5934–5942, DOI: 10.1039/c3ta10349h.

30 X. L. Wu, L. Wang, C. L. Chen, A. W. Xu and X. K. Wang, Water-dispersible magnetite-graphene-LDH composites for efficient arsenate removal, *J. Mater. Chem.*, 2011, **21**, 17353–17359, DOI: 10.1039/c1jm12678d.

31 S. Barkhordari and A. Alizadeh, Fabrication of pH-sensitive chitosan/layered double hydroxide (LDH)/Fe_3O_4 nanocomposite hydrogel beads for controlled release of diclofenac, *Polym. Bull.*, 2022, **79**, 5533–5548, DOI: 10.1007/s00289-021-03761-3.

32 X. Hong, C. Ding, M. Shi, Z. Ding, P. Du, M. Xia and F. Wang, Easy separation dual-function Cu_2O@LDH@Fe_3O_4 adsorbent for the removal of Cr(VI) under dark conditions: experimental and mechanistic study, *Sep. Purif. Technol.*, 2024, **332**, 125734, DOI: 10.1016/j.seppur.2023.125734.

33 Y. You, G. Xu, X. Yang, Y. Liu, X. Ma and Y. Ji, Cu–Fe–Ni layered hydroxides/magnetic biochar composite as peroxymonosulfate activator for removal of enrofloxacin, *Colloids Surf., A*, 2024, **683**, 133082, DOI: 10.1016/j.colsurfa.2023.133082.

34 D. Chen, Y. Li, J. Zhang, J. Z. Zhou, Y. Guo and H. Liu, Magnetic Fe_3O_4/ZnCr-layered double hydroxide composite with enhanced adsorption and photocatalytic activity, *Chem. Eng. J.*, 2012, **185–186**, 120–126, DOI: 10.1016/j.cej.2012.01.059.

35 M. Hossein Beyki, M. Mohammadirad, F. Shemirani and A. A. Saboury, Magnetic cellulose ionomer/layered double hydroxide: an efficient anion exchange platform with enhanced diclofenac adsorption property, *Carbohydr. Polym.*, 2017, **157**, 438–446, DOI: 10.1016/j.carbpol.2016.10.017.

36 R. Massart, Preparation of Aqueous Magnetic Liquids in Alkaline and Acidic Media, *IEEE Trans. Magn.*, 1981, **17**, 1247–1248.

37 A. L. Patterson, The Scherrer formula for X-ray particle size determination, *Phys. Rev.*, 1939, **56**, 978–982, DOI: 10.1103/PhysRev.56.978.

38 J. Park and J. R. Regalbuto, A Simple, Accurate Determination of Oxide PZC and the Strong Buffering Effect of Oxide Surfaces at Incipient Wetness, *J. Colloid Interface Sci.*, 1995, **175**(1), 239–252, DOI: 10.1006/jcis.1995.1452.

39 B. H. Toby and R. B. Von Dreele, GSAS-II: the genesis of a modern open-source all purpose crystallography software package, *J. Appl. Crystallogr.*, 2013, **46**, 544–549, DOI: 10.1107/S0021889813003531.

40 A. V. Samrot, C. S. Sahithya, J. Selvarani A, S. K. Purayil and P. Ponnaiah, A review on synthesis, characterization and potential biological applications of superparamagnetic iron oxide nanoparticles, *Curr. Res. Green Sustainable Chem.*, 2021, **4**, 100042, DOI: 10.1016/j.crgsc.2020.100042.

41 T. Arun, K. Prakash and R. Justin Joseyphus, Synthesis and magnetic properties of prussian blue modified Fe nanoparticles, *J. Magn. Magn. Mater.*, 2013, **345**, 100–105, DOI: 10.1016/j.jmmm.2013.05.058.

42 M. Thommes, K. Kaneko, A. V. Neimark, J. P. Olivier, F. Rodriguez-Reinoso, J. Rouquerol and K. S. W. Sing, Physisorption of gases, with special reference to the evaluation of surface area and pore size distribution (IUPAC Technical Report), *Pure Appl. Chem.*, 2015, **87**, 1051–1069, DOI: 10.1515/pac-2014-1117.

43 H. C. B. Hansen and R. M. Taylor, Formation of synthetic analogues of double metal-hydroxy carbonate minerals under controlled pH conditions: I. The synthesis of pyroaurite and reevesite, *Clay Miner.*, 1990, **25**, 161–179.

44 Y. S. Ho and G. McKay, Pseudo-second order model for sorption processes, *Process Biochem.*, 1999, **34**(5), 451–465, DOI: 10.1016/S0032-9592(98)00112-5.

45 W. J. Weber and J. C. Morris, Kinetics of adsorption carbon from solutions, *J. Sanit. Eng. Div., Am. Soc. Civ. Eng.*, 1963, **89**, 31–59.

46 C. H. Giles, D. Smith and A. Huitson, A general treatment and classification of the solute adsorption isotherm. I. Theoretical, *J. Colloid Interface Sci.*, 1974, **47**, 755–765, DOI: 10.1016/0021-9797(74)90252-5.

47 O. Redlich and D. L. Peterson, A useful adsorption isotherm, *J. Phys. Chem.*, 1959, **63**, 1024, DOI: 10.1021/j150576a611.

48 K. H. Chu, Revisiting the Temkin Isotherm: Dimensional Inconsistency and Approximate Forms, *Ind. Eng. Chem. Res.*, 2021, **60**, 13140–13147, DOI: 10.1021/acs.iecr.1c01788.